Comparison of Turbulence Kinetic Energy Dissipation Rate Estimates from Two Ocean Microstructure Profilers

J. N. MOUM

College of Oceanic and Atmospheric Sciences, Oregon State University, Corvallis, Oregon

M. C. GREGG AND R. C. LIEN

Applied Physics Laboratory, University of Washington, Seattle, Washington

M. E. CARR

College of Oceanic and Atmospheric Sciences, Oregon State University, Corvallis, Oregon

(Manuscript received 1 April 1994, in final form 9 September 1994)

ABSTRACT

Almost 1000 microstructure profiles from two separate groups on two separate ships using different instrumentation, signal processing, and calibration procedures were compared for a 3.5-day time period at 0°, 140°W and within 11 km of each other. Systematic bias in the estimates of ϵ is less than a factor of 2, which is within estimates of the cumulative uncertainties in the measurement of ϵ.

Although there is no evidence for strong gradients in mean currents, water properties, or surface meteorology, occasional hourly averages of ϵ differ by several factors of 10. Both groups observed periods where ϵ estimates exceeded those of the other group by large factors. The authors believe that the primary reason for these large differences is natural variability, which appears to be greater in the meridional direction than in the zonal direction.

1. Introduction

Although oceanic estimates of the turbulence dissipation rate of kinetic energy ϵ have been made by several groups over the past 20 years, there has been little opportunity to make direct comparisons between groups. This has largely been due to logistical constraints and the great amount of time and energy required to mount a sea-going experiment. However, all of the groups making the measurements from which ϵ is estimated have very different experimental configurations, different means of calibrating sensors, and different analog and digital signal processing procedures. As a result, there are many sources of uncertainty in the estimates of ϵ and many ways that estimates may differ between groups. In fact, a rudimentary comparison of ϵ estimates from the first Tropic Heat experiment in 1984 (Moum and Caldwell 1985; Gregg et al. 1985; Moum et al. 1989) indicated a *systematic* difference between the two groups involved (Peters et al. 1988).

Corresponding author address: Dr. Jim Moum, College of Oceanic and Atmospheric Sciences, Oregon State University, Oceanography Admin. Bldg. 104, Corvallis, OR 97331-5503.

As defined in the Reynolds-averaged turbulence kinetic energy (TKE) equation, the TKE dissipation rate is

$$\epsilon = \nu(T)\,\overline{\frac{\partial u_i}{\partial x_j}\left(\frac{\partial u_i}{\partial x_j} + \frac{\partial u_j}{\partial x_i}\right)}. \qquad (1)$$

Here $\nu(T)$ is the temperature-dependent kinematic viscosity of the fluid [in seawater $\nu(T)$ is weakly dependent on salinity and pressure but strongly dependent on temperature; in equatorial waters the temperature ranges from 28°C at the surface to 10°C at 200-m depth, causing a 50% variation in $\nu(T)$]; u refers to the turbulence velocity fluctuations; x refers to the spatial coordinate system; and standard tensor notation is used, summing over three components. The overbar refers to a suitable average that is not usually realized in field measurements. Ideally, the overbar represents an average over a large number of representative examples of the turbulence (an ensemble average). From vertical profiles, however, the data represent a vertical series through a turbulent field of unknown horizontal dimension at some unknown stage of temporal evolution. From this, we compute an average over a finite depth extent.

The fundamental measurement used to estimate (1) is accomplished using airfoil (shear) probes (Osborn

and Crawford 1980). These sense the velocity fluctuations in a coordinate orthogonal to the flow direction. Two sensors mounted with their sensing elements aligned orthogonally resolve the horizontal velocity fluctuation field. The probe signal is routinely differentiated electronically. The process of differentiation

(i) emphasizes the high-frequency part of the signal that contributes the most to ϵ,

(ii) removes the low-frequency part of the signal that is not particularly useful because of the inherent ac properties of peizoceramic devices, the large and variable temperature sensitivity of the devices, and the high-pass filtering affected due to the finite size of profilers moving vertically through the flow field, and

(iii) thereby permits sampling a greater dynamic range of the signal of interest.

Using Taylor's frozen flow hypothesis (that is, time derivatives are equivalent to spatial derivatives in the direction of the mean flow if the flow field evolves slowly relative to the time period over which it is measured) and the flow speed past the probe, the spatial derivatives of the velocity fluctuations are obtained. From vertically profiling microstructure instruments such as CHAMELEON and AMP,[1] the flow speed past the probe is approximated by the rate at which the profiler falls through the water column. The spatial derivatives obtained are $\partial u/\partial z$ and $\partial v/\partial z$. These represent 2 of 12 terms in (1); for isotropic turbulence, the terms are simply related, only one dependent term exists (Hinze 1975) and the following approximation to (1) is made:

$$\epsilon \approx \frac{15}{4}\nu\left[\overline{\left(\frac{\partial u}{\partial z}\right)^2} + \overline{\left(\frac{\partial v}{\partial z}\right)^2}\right]. \qquad (2)$$

Since $\overline{(\partial u/\partial z)^2} \approx \overline{(\partial v/\partial z)^2}$ for isotropic turbulence, two probes mounted parallel (that is, mounted so as to sense the same component of velocity fluctuation) might also be used to obtain $\epsilon \approx (15/2)\nu\overline{(\partial u/\partial z)^2} \approx (15/2)\nu\overline{(\partial v/\partial z)^2}$. In a stratified fluid, some degree of anisotropy of the turbulence may exist at low values of the parameter $\epsilon/\nu N^2$ [$N^2 = -(g/\rho)(\partial\rho/\partial z) - (g^2/c^2)$; g is the gravitational constant, ρ is the density of seawater, c is the speed of sound in seawater; and z is the vertical coordinate]. Anisotropy becomes more evident as ϵ diminishes relative to the stratification. Recent work by Itsweire et al. (1993), Thoroddsen and Van Atta (1992), and Yamazaki and Osborn (1990) has sought to quantify the effect of anisotropy on ϵ estimates. We cannot address this problem here as we have no way to test the isotropic assumptions from our data. According to Yamazaki and Osborn (1990), the isotropic estimate is reasonable for $\epsilon/\nu N^2 > 20$, and this condition is satisfied for most of the data examined in this study (Fig. 1; particularly 50-, 75-, 100-, and 125-m depths).

As part of the Tropical Instability Wave Experiment (TIWE), we endeavoured to occupy a station at 0°, 140°W for a period that would include two full cycles of the 21-day (nominal) period tropical instability waves under investigation. Because of limited ship duration, two ships (and groups) were required to make the measurements, the plan being to combine the two datasets into a single continuous dataset following the experiment. A 3.5-day overlap period was planned into the operations so that data comparisons could be made before combining datasets. During this time, the two groups profiled continuously within several kilometers of each other.

The purpose of this paper is to assess the uncertainties in estimates of ϵ made by the two groups while in close proximity to each other. This is done by statistical comparisons of the two datasets, which is discussed in the main text of the paper. The details of the instrumentation, calibrations, and both hardware and software processing techniques used by each group are described in separate appendices. The appropriateness of the use of a universal spectral form for dissipation range

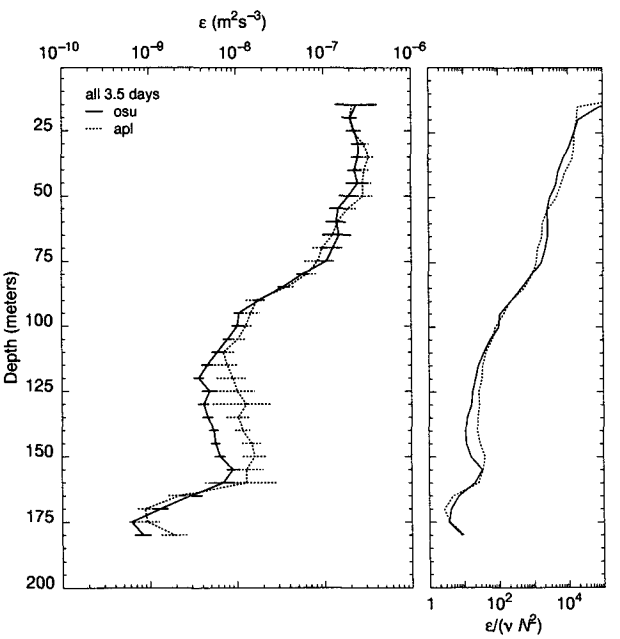

FIG. 1. Averaged ϵ profiles at 5-m intervals for the 3.5-day overlapping time series from the OSU group (solid line) and the APL/UW group (dashed line). The 95% confidence intervals of the mean values at each depth were computed using the bootstrap method. Also shown are profiles of the isotropy parameter $\epsilon/\nu N^2$ determined from each dataset.

[1] CHAMELEON was designed, constructed, and deployed by the microstructure group at the College of Oceanic and Atmospheric Sciences, Oregon State University; hereafter OSU. AMP (advanced microstructure profiler) was designed, constructed, and deployed by the microstructure group at the Applied Physics Laboratory, College of Ocean and Fishery Sciences, University of Washington; hereafter UW.

turbulence as a correction factor for incomplete measurement resolution of the spectrum is discussed in appendix C.

2. Results

The TIWE provided the opportunity for an extensive comparison of microstructure measurements between the UW and OSU groups. One purpose of the experiment was to resolve two cycles of the 21-day tropical instability waves that have been observed in most boreal autumns. The endurance of most suitable ships in the research fleet is limited to 35–40 days by a combination of fuel, food, labor regulation, and psychological considerations. Steaming time from Honolulu to the station at 0°, 140°W is about 6 days. This meant that two ships (and two groups) were required to maintain a continuous station for at least 42 days.

The R/V *Wecoma,* carrying the OSU group, arrived on station at about 1700 UTC 4 November 1991 (local time is about UTC − 10 h; 4 November corresponds to year-day 308 with 1 January counted as day 1). CHAMELEON was deployed on a nearly continuous basis from then until 2400 UTC 24 November at the rate of 8–12 profiles per hour to 200-m depth. Profiling was done from the stern of the ship, while steaming was at about 0.2 m s^{-1} relative to the water. To avoid going farther than 5.5 km from the NOAA (National Oceanic and Atmospheric Administration) buoy at the station (from which hourly range and bearing readings were made) and to maintain continuous measurements, this method required us to profile while heading both into and away from the wind. Disruptions in profiling were mainly due to the maintenance schedule determined by the engineering department of R/V *Wecoma,* requiring two hours of steaming at about lunchtime every other day and by occasional instrumentation problems.

The R/V *Moana Wave,* carrying the UW group, arrived on station and began profiling at about 1500 UTC 21 November 1991 and stayed until 13 December, deploying AMP at a profiling rate of two to four profiles per hour. AMP was deployed from the starboard side of *Moana Wave,* with the wind on the starboard side so that the ship drifted away from the profiler at all times. Disruptions in profiling were mainly due to repositioning of the ship upwind of the NOAA buoy once the ship had drifted too far downwind from the buoy.

A detailed description of the upper ocean over the entire overlapped period, including hydrography and current structure, is given by Lien et al. (1995).

The period of overlap of the two groups on station was almost 3.5 days, during which hourly range and bearing estimates were made from *Wecoma* to determine the relative position of *Moana Wave.* Many hundreds of comparison profiles were made with the ships within 1–11 km of each other. For comparison, the data were averaged vertically over 5 m and centered at 15, 20, 25 m, etc. Time-averaged vertical profiles were plotted at these depths. For direct data comparisons, we concentrated our analysis at four depths: 50, 75, 100, and 125 m.

The first comparison of the two datasets consists of vertical profiles averaged vertically over 5 m and over the entire 3.5-day time series (Fig. 1). These agree within 95% bootstrapped confidence intervals at 27 of 34 depth intervals. The AMP estimates were consistently higher over 120–150 m. An examination of ϵ time series showing data from each individual AMP and CHAMELEON profile at fixed depths shows two important features (Fig. 2). First of all, the longer period (more than several hours) trends are clearly coherent in the two series. A diurnal mixing cycle is evident at 50 m, peaking at or shortly after 1200 UTC (0.5 decimal day time), coincident with maximum nighttime cooling. The cycle was more pronounced during the latter two days of the record, when the wind stress was greater (wind stress was greater than 0.1 N m^{-2} after 327.0, but less than 0.08 N m^{-2} prior to that, dipping below 0.02 N m^{-2} between 326.3 to 326.6). At 75-m depth the sharp increase in ϵ shortly after 327.5 was observed at both ships. Although the sharp change appeared in both datasets, the nature of the change was different in each dataset. With the exception of a single point, the ϵ values observed by CHAMELEON were more than two orders of magnitude greater than those observed by AMP after the change. In fact there are many examples in the time series where short period (hours) increases in ϵ were observed at one ship but not the other. For example, on day 326.5 at 50-m depth, the UW group aboard *Moana Wave* observed ϵ values that were 10–100 times greater than observed by the OSU group on *Wecoma.* Shortly after 328.5 at 125 m, the OSU group observed ϵ values that were 10–100 times greater than were observed by the UW group. Incidents of periods when sustained large ϵ was sensed by one group but not the other seem to be equally apportioned between groups.

Histograms of the data (Fig. 3; all profiles included individually) show that even though the mean values at most depths correspond within 95% confidence limits, distributions of the data do not usually agree so well. At 75-m depth probability distributions of the two datasets pass the χ^2 test at the 99% significance level, indicating that the values are representative of the same population. At other depths, the χ^2 statistic is high, indicating that the distributions differ. At 50 m, the CHAMELEON average is dominated by fewer, higher values of ϵ. Below 75 m, the different noise levels of the two estimates contribute to the high χ^2 statistic, as seen in the histogram at 125-m depth. The noise level for CHAMELEON is apparently somewhat larger than for AMP, as seen in the peaks in the histogram at several times 10^{-10} m^2 s^{-3} (although 40%–50% of the values are within a factor of 3 of the noise peak,

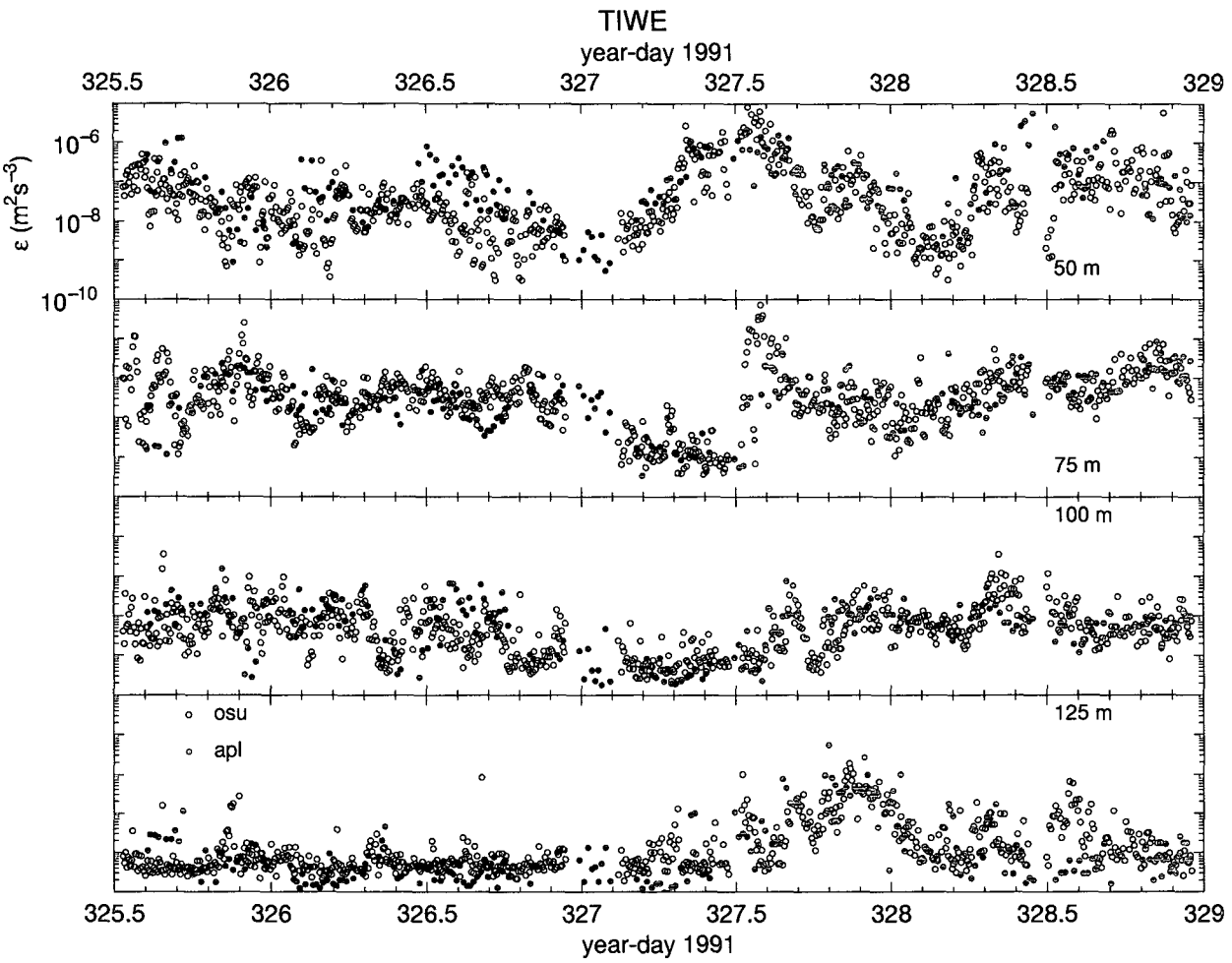

FIG. 2. Time series of ϵ (5-m averages) from every AMP (filled circle) and CHAMELEON (open circle) profile during the 3.5-day overlap period at 50, 75, 100, and 125 m.

the arithmetic mean value of ϵ at that depth is determined by the few values above 10^{-8} m^2 s^{-3}, as seen in the lower panel of Fig. 3d). The differences in noise levels may be accounted for by the differences in fall speeds of the two profilers as they were set for TIWE (see discussion in appendix A and Figs. A5, A6, B7).

For a direct one-to-one comparison of the two datasets, all of the profiles in a 1-h period were averaged together (8–12 CHAMELEON profiles; 2–4 AMP profiles), and this value was assigned to the hour (hourly averaged time series are shown in Fig. 4). The resulting data pairs were further compared statistically in scatterplot form and also in a comparison of the ratios of data pairs (Fig. 5). The two series are significantly correlated at all depths (for 80 data pairs, the 95% significance level for the linear correlation coefficient is 0.22; Bendat and Piersol 1986). However, occasional data pairs differ by a factor of 100 or more, 15% differ by more than a factor of 10 at 50 m, 9% at 75 m, 6% at 100 m, and 14% at 125 m.

Daily averaged profiles of ϵ from the two groups (Fig. 6) suggest that the good agreement illustrated in Fig. 1 may have been fortuitous. The differences in daily averages are substantially larger than found in the 3.5-day average. Above 60-m depth on the first day of the comparison, the two means differed by up to a factor of ten, while the 3.5-day means were not significantly different (within 95% confidence limits). On day 1, only 15 of 34 depth averages agreed within 95% confidence limits, compared to 30 of 34 on both of days 2 and 3.

3. Discussion

There are significant similarities between these two datasets, but there are also some important differences. Our primary objective was to assess the cumulative effect of measurement uncertainty on the reduced data. However, is it possible that the natural intermittency of turbulent flows and the spatial and temporal dis-

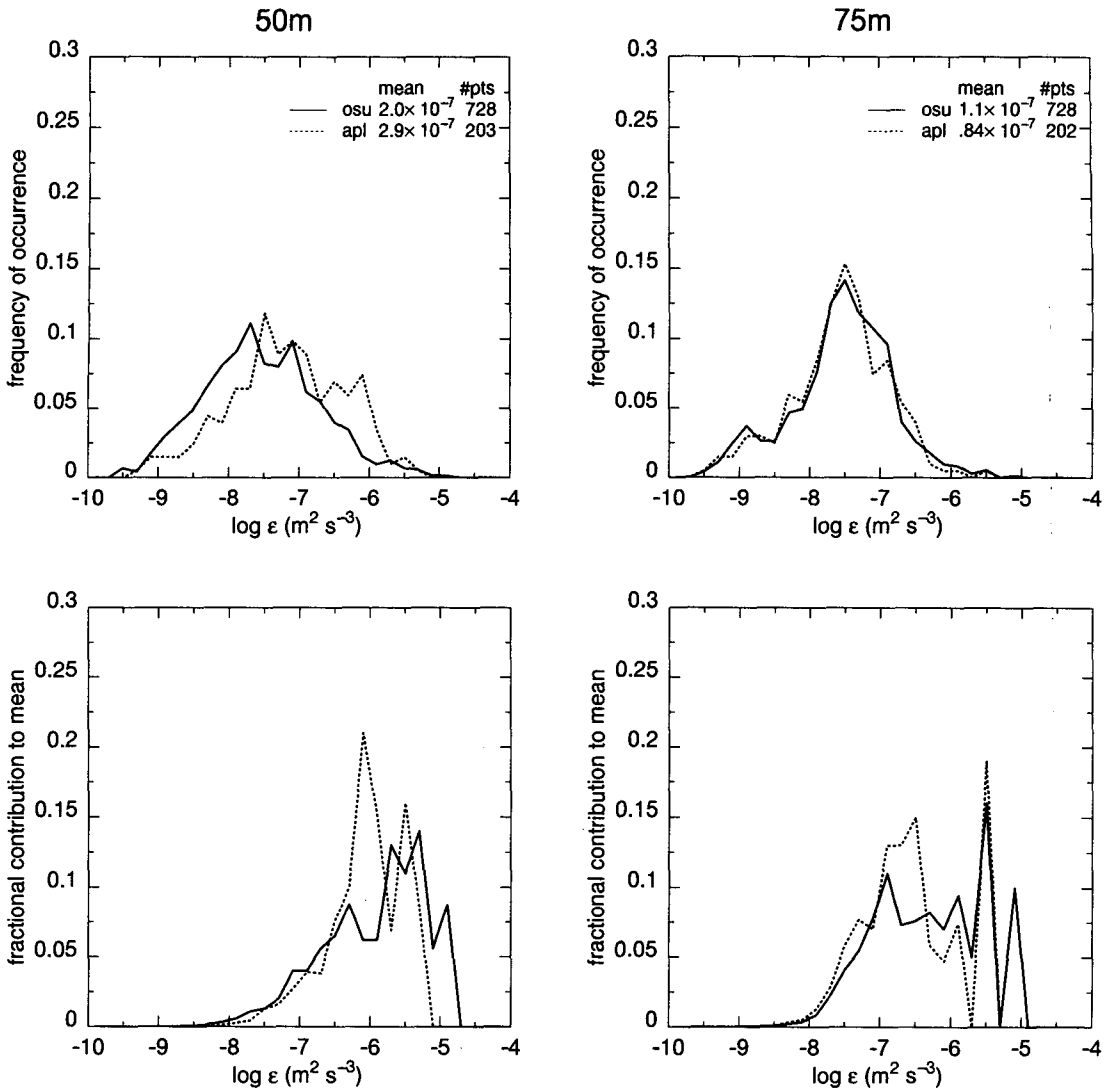

FIG. 3. Histograms and fractional contributions to the arithmetic mean for the data shown in Fig. 2. The fractional contribution was determined as the product of the ordinate and the abscissa in each bin in the upper panel divided by the mean value for the dataset.

parities in the measurements dominate the differences in the datasets? Let us begin by reviewing the results from the data comparison for ϵ.

1) Mean values at almost all depths agree within 95% confidence limits when averaged over the entire overlap period. However, daily averages exhibit large differences, especially in the upper 60 m.

2) Histograms generated from all of the data are statistically identical at 75 m but differ at 50, 100, and 125 m. At 100 and 125 m, this is largely due to differing noise levels in the two estimates of ϵ.

3) Direct comparisons of hourly averaged data reveal significant correlations at all depths.

4) Even though individual data pairs occasionally differ by more than a factor of 10, the majority of the ratios were less than a factor of 3; modes are clustered near 1.

Points 2 and 3 suggest that there is good general agreement between the two datasets. There is no evidence for systematic bias due to measurement error. The occasional large differences noted in 4 are primarily responsible for the differences in averages over timescales less than the entire overlap period. Since the data have been carefully screened, both objectively and subjectively, we have no reason to believe that there remains any source of intermittent contamination (such as described in the appendices) that would cause the large differences. Consequently, we believe that the remaining differences between the two datasets are due to natural variability in the turbulence.

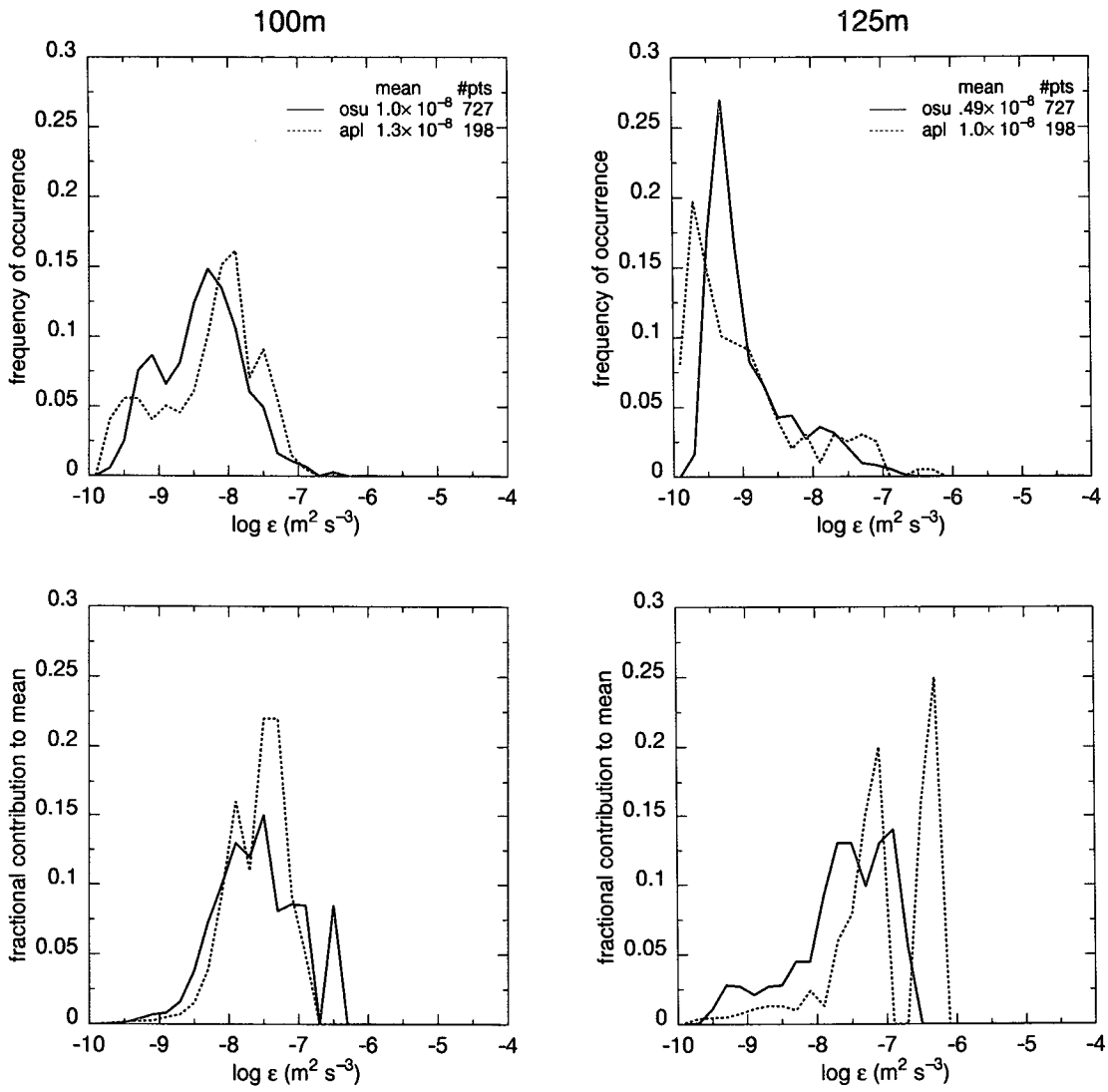

FIG. 3. (*Continued*)

Any assessment of natural variability in the flow is difficult to make given the limited data. We really only have 80 data pairs to evaluate. The number of degrees of freedom must be substantially less than this since the variability in ϵ is mainly due to diurnal variations and to events with several hours duration. On the other hand, some points seem clear. The most important is the fact that we have to consider the close agreement of the averaged vertical profiles of ϵ to be somewhat fortuitous. None of the daily averages agree nearly so well as the 3.5-day averages (at least above 60 m), especially on the first day of the comparison (326.0–327.0) when the averaged values of ϵ differed by up to a factor of 10 above 60 m (Fig. 6a). The time series at 50 m (Fig. 4) clearly shows the period (near 326.5) when the AMP estimates were consistently in excess of those from CHAMELEON. Since the instrumentation and signal processing was unchanged from the rest of the experiment, and there were also periods when CHAMELEON estimates exceeded AMP estimates by similar amounts (although over shorter time periods), we have no reason to expect any other factor than natural variability of the turbulence in the flow field. We conclude that natural variability can cause large differences in averages of ϵ made over coincident $O(100+)$ profiles spaced reasonably evenly over the sampling period and located within several km of each other. It may be only coincidental that the estimates of ϵ from the latter two days of the comparison (Figs. 6b,c) counteract the trend from the first day to produce the apparent excellent agreement in the 3.5-day averages (Fig. 1). Alternatively, perhaps 3.5 days was the appropriate timescale for resolving the variability at that particular time and place.

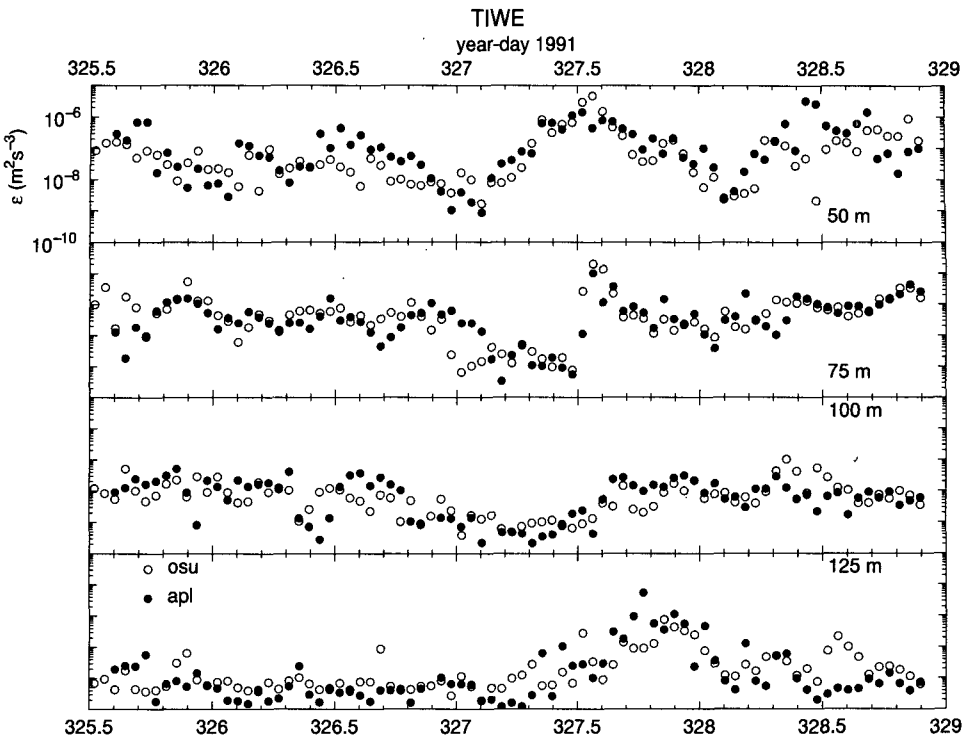

FIG. 4. Time series of hourly averaged ϵ from the data shown in Fig. 2. AMP data are represented by bullets and CHAMELEON data by open circles.

Two aspects of the sampling that we can relate to natural variability are the effects of the separation between and relative orientation of the two ships from which measurements were made. A simple analysis to determine the relative influence of ship positions was performed. While on station, hourly range and bearing measurements to *Moana Wave* were made by the bridge officers on *Wecoma* using the ship's radar. We used this information to subsample the hourly averaged data pairs into periods when the ships were close together (<5.5 km) and farther apart (>5.5 km) and also into periods when the ships were aligned predominantly north–south (that is, when the bearing from *Wecoma* to *Moana Wave* was within either of the ranges 315°–045° or 135°–225°) or east–west (bearing 045°–135° or 225°–315°, *Wecoma* to *Moana Wave*). The comparison is summarized in Table 1. Above 125 m, correlations between the two datasets were clearly enhanced (with 95% confidence) when the ships were aligned more zonally than meridionally. This depth range encompasses the high-shear, low-Richardson number region of the Equatorial Undercurrent. In contrast, the relative separations between the two ships had much less effect than the relative orientation; correlation coefficients were not different at the 95% significance level. Grouping the close data (<5.5 km) into east–west and north–south orientations resulted in a somewhat higher distinction between east–west and north–south orientations at 75 and 100 m (though not at 50 m), but the small numbers of points precluded computation of confidence limits.

This analysis suggests a preferred orientation of turbulence structures in the upper equatorial ocean. Either turbulent structures are advected east–west (in the direction of the mean flow) rapidly enough that they persist over several kilometers or instabilities that force the turbulence in the low-Richardson number flow field (Moum et al. 1992) propagate preferentially east–west, leaving turbulence in their wake. This aspect is the subject of more intensive investigation of the TIWE datasets.

Given this particular example showing large spatial variability in ϵ over separations of a few kilometers, we have to consider the possibility that differences observed in the Tropic Heat 1 experiment, in which separations were considerably larger (20–30 km), were due largely to natural variability in the field. We should continue to be aware of this in interpreting any microstructure datasets, past or future.

4. Summary

A comparison of almost 1000 microstructure profiles from two separate groups on two separate ships using different instrumentation, signal processing, and calibration procedures was made for a 3.5-day time period at 0°, 140°W and within 11 km of each other. We conclude that any systematic bias in the estimates of ϵ

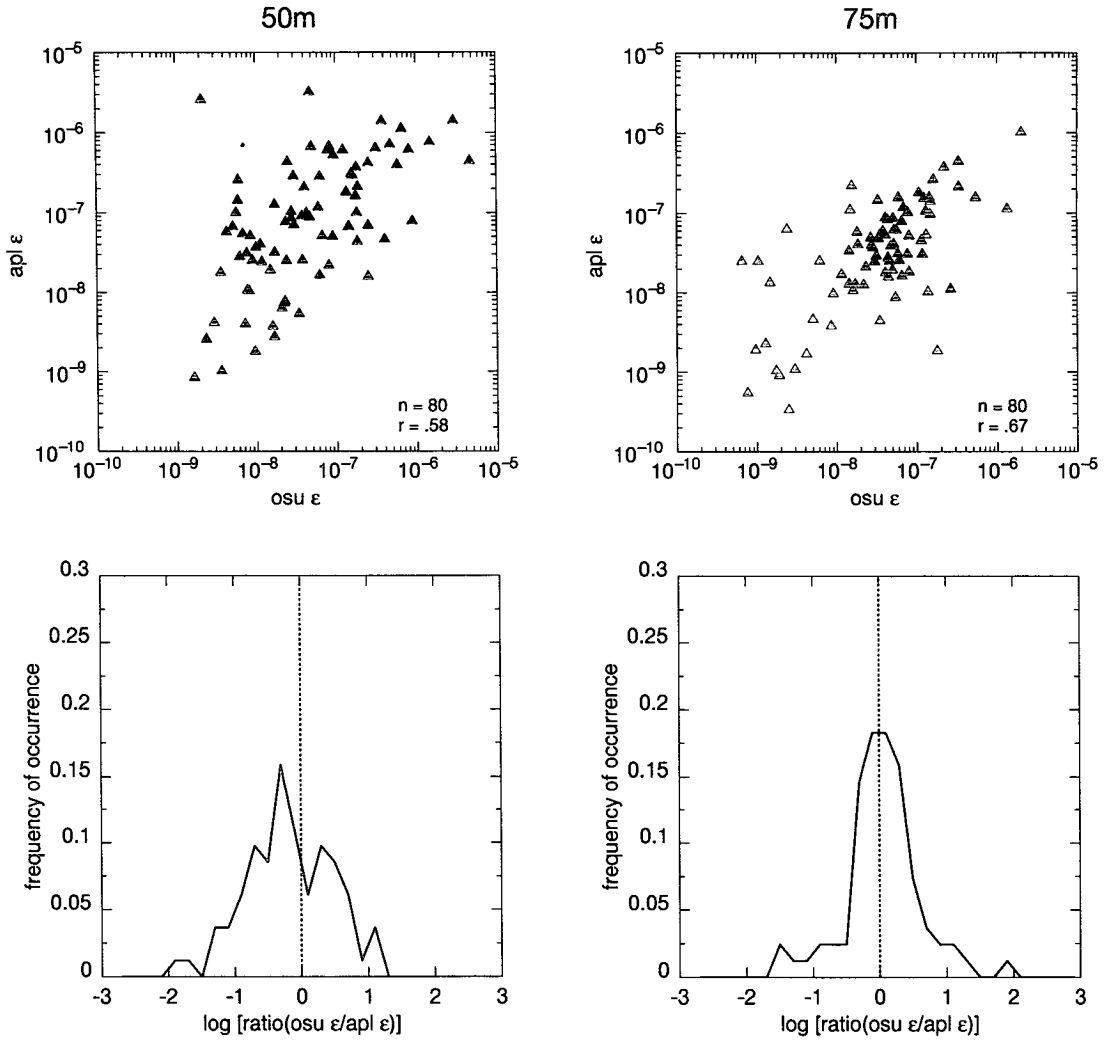

FIG. 5. Scatterplots of hourly averaged data appearing in Fig. 4 and histograms of the log of the ratio of the two estimates of ϵ. The number of points n in each sample population and the correlation coefficient r between the two variables are shown in the upper panel for each depth.

is less than a factor of 2, within our estimates of the cumulative uncertainties in the measurement of ϵ [when the isotropic formulation (2) is valid].

Although there is no evidence for strong gradients in mean currents, water properties, or surface meteorology, there are occasional hourly averages of ϵ that differ by several factors of 10. Both groups observed periods where ϵ estimates exceeded those of the other group by large factors. We believe that the sole reason for large differences in the ϵ data from the two groups is natural variability. The variability appears to be greater in the meridional direction than in the zonal direction.

Acknowledgments. The AMP observations were made possible by the skill and dedication of Jack Miller, Steve Bayer, Wayne Nodland, Dale Hirt, Lisa Bogar, Earl Krause, Tom Lehman, Keith Brainerd, and Gordy Welsh. At OSU, we are grateful to Mike Neeley-Brown, Ray Kreth, Jose Baer, and Ed Llewelyn for their engineering expertise in helping to develop CHAMELEON hardware, software, and calibration facilities. The collection of these data is labor intensive. We would also like to thank Chaojiao Sun, Dave Hebert, John Lien, Vasillis Zervakis, Pat Collier, and Mary Mooney for their help at sea. This work was funded by the National Science Foundation (OCE-8816098 to OSU and OCE-9202773 to UW).

APPENDIX A

CHAMELEON

CHAMELEON is 4 m long by 0.064 m in diameter (Fig. A1). The vehicle is loosely tethered to the sur-

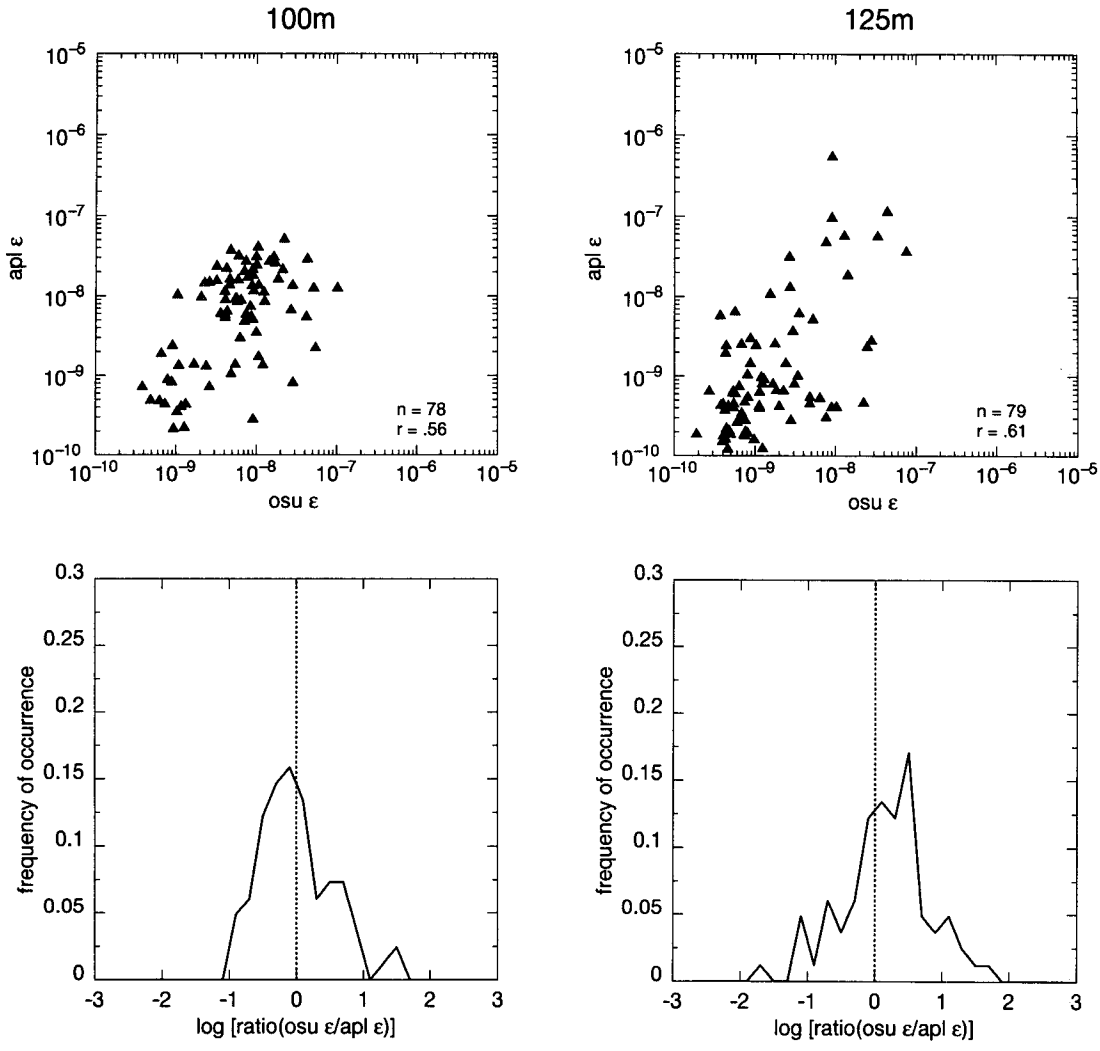

FIG. 5. (*Continued*)

face by a 0.0044-m-diameter, two-conductor jacketed cable with a Kevlar core for tensile strength. This cable is negatively buoyant. CHAMELEON freely falls through the water column (at speeds that can be varied by adjusting weights and drag). To operate in the strong equatorial current shear (see discussion in appendix B), extra weight and drag were added to CHAMELEON, and the terminal fall speed consequently increased from our normal operating speed of 0.8 to 1.2 m s^{-1} (see Fig. A6), decreasing to approximately 1 m s^{-1} at 200 m. Body motion is monitored by accelerometers mounted inside. Once terminal depth has been reached, CHAMELEON is retrieved using a winch mounted at the ship's stern. To ensure that CHAMELEON does not become entangled in the ship's propulsion or steering mechanisms, a small amount of way is maintained by the ship. Hence, the profiler initially falls through the ship's wake, and we do not consider data above 10 m for analysis here.

Power is supplied by lithium D-cell batteries inside of CHAMELEON. The 16 channels of sensor data are processed by internal analog electronics, sampled by a 16-bit A/D converter, and transmitted electrically at a rate of 76.8 kbaud up the data cable for storage on a PC-compatible computer. Further analysis is performed on SPARC workstations.

a. Sensors

The OSU shear sensor design is shown in Fig. A2. A 0.019-m-long peizobimorph ceramic sensing element is fitted into a machined Teflon insert, which in turn is sealed (O-ring bore seal) and potted into a 0.0064-m-diameter stainless steel sting. The Teflon acts to effectively prevent low-level seawater leaks to the high-impedance probe. Although the Teflon also stiffens the

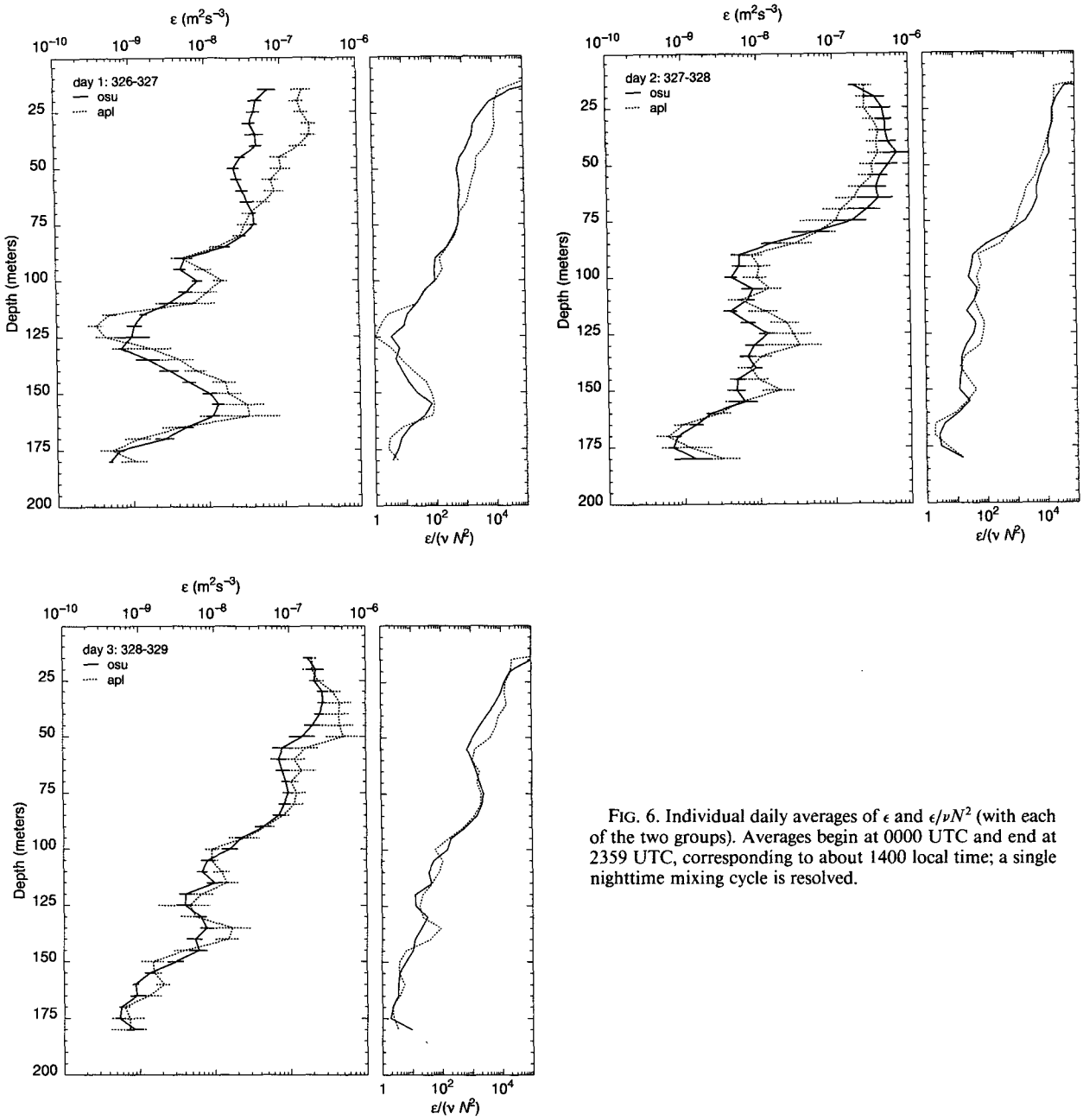

FIG. 6. Individual daily averages of ϵ and $\epsilon/\nu N^2$ (with each of the two groups). Averages begin at 0000 UTC and end at 2359 UTC, corresponding to about 1400 local time; a single nighttime mixing cycle is resolved.

sensing element, making it less sensitive to signal, experience shows that this is not a limiting factor in sensing turbulent velocity shear fluctuations; rather, hydrodynamically induced body motions determine the noise level of ϵ (see following discussion). At the sensing end of the device, the Teflon holder and beam are potted into a silicone rubber compound in the shape of a paraboloid of revolution (0.025 m long). The sting is 0.19 m long and is fitted with a jack for plugging into the Delrin nose cone of CHAMELEON. The total cross force on the probe is given by Osborn and Crawford (1980) as

$$F = \rho A W u', \tag{A1}$$

where ρ is water density, A is the cross-sectional area perpendicular to the flow, W is the flow velocity along the axis of the probe, and u' is the cross-flow velocity. This can be written as

$$F = \frac{1}{2}\rho V^2 A \sin 2\alpha, \tag{A2}$$

where V is the total flow speed and α the angle of attack of the probe relative to V.

b. Calibration

The OSU calibration facility is modeled after that described by Osborn and Crawford (1980). The probe is mounted vertically with the sensing end in the nozzle of an upward-flowing axisymmetric jet. The flow is squeezed by an exponential contraction upstream of the nozzle to ensure a reasonably flat velocity profile at the nozzle. The flow velocity is measured with an in-line impeller flowmeter. The probe is rotated about its axis of symmetry at 6 Hz, while the output voltage is sampled and varied over a range of attack angles to provide a range of cross-flow velocities. The probe output voltage (rms) is measured and related to V, α by

$$E_{\text{rms}} = \rho S V^2 \sin 2\alpha, \qquad \text{(A3)}$$

where S is the probe sensitivity [V (N m^{-2})$^{-1}$]. Sensitivity S is then determined as the best fit to a regression of $E_{\text{rms}}/\rho V^2$ versus $\sin 2\alpha$. Equations (A1), (A2), (A3), and (B1) give the correspondence between the sensitivities determined by the OSU and UW groups as

$$S = \frac{S_v}{4\sqrt{2}\rho g}. \qquad \text{(A4)}$$

Here S [V (N m^{-2})$^{-1}$] is the OSU probe sensitivity and S_v (V m^{-1}) is the UW probe sensitivity. All probes used in this experiment were run through the calibration procedure twice before the cruise and twice after the cruise. However, the precruise calibrations were clearly of poor quality (for unknown reasons) and do not agree with long-term histories of individual probes. Generally, 15% deviations between individual calibrations is considered large. Deviations from TIWE precruise calibrations were considerably larger than this.

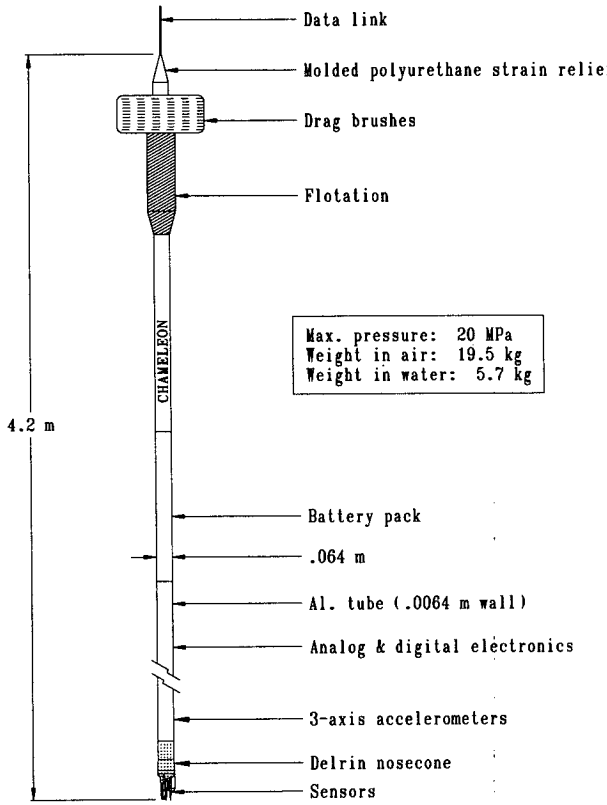

FIG. A1. Schematic of CHAMELEON.

Postcruise calibrations are in general agreement with long-term probe histories and were used for analysis.

c. Signal processing

The analog circuitry for processing the signal from the OSU shear probes consists of a high-impedance buffer

TABLE 1. Correlation coefficients computed between OSU and APL/UW ϵ data (hourly averages) at the nominal depths used for analysis (second column) are shown. The data were further sorted into groupings where the two ships were aligned in east–west (bearing 045°–135°, 225°–315°) and north–south (bearing 315°–045°, 135°–225°) quadrants and into groupings where the separation between ships was less than 5.5 km and greater than 5.5 km; for those points where the separation was less than 5.5 km, the correlation coefficients were again computed for east–west and north–south quadrant groupings. In parentheses are 95% confidence limits computed using the bootstrap method. Because the datasets defined in the last two columns had only 15 data points apiece, no confidence limits were computed. For 15 data pairs, the 95% significance level of the linear correlation coefficient is 0.51 (Bendat and Piersol 1986).

		All data		All data		< 5.5 km	
	All data	east–west	north–south	< 5.5 km	> 5.5 km	east–west	north–south
50 m	0.56 (0.40, 0.69)	0.70 (0.57, 0.81)	0.19 (−0.15, 0.51)	0.63 (0.45, 0.79)	0.47 (0.22, 0.67)	0.62	0.47
75 m	0.67 (0.52, 0.80)	0.84 (0.74, 0.92	0.44 (0.20, 0.65)	0.84 (0.71, 0.93)	0.72 (0.54, 0.85)	0.91	0.30
100 m	0.54 (0.38, 0.67)	0.68 (0.51, 0.81)	0.14 (−0.31, 0.52)	0.64 (0.39, 0.82)	0.40 (0.12, 0.63)	0.82	0.28
125 m	0.60 (0.45, 0.71)	0.53 (0.36, 0.67)	0.73 (0.41, 0.93)	0.64 (0.41, 0.82)	0.61 (0.46, 0.74)	0.47	0.82

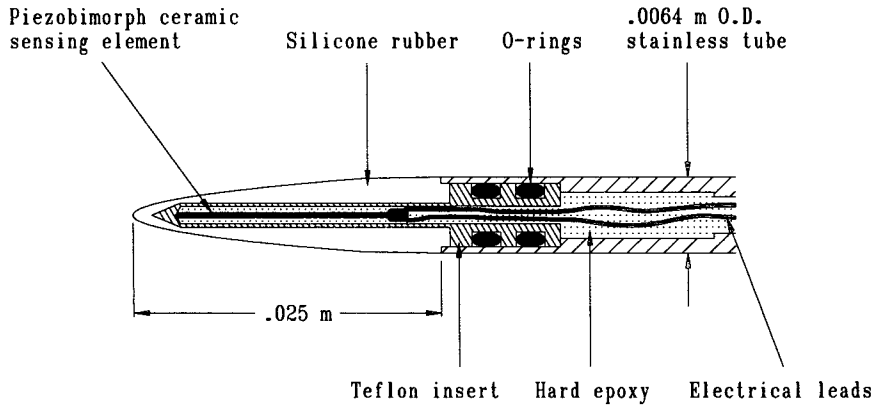

FIG. A2. Schematic of airfoil probe used by the Oregon State University group.

($R_0 = 10^{10}\Omega$ in Fig. A3) and a 1.5-s time constant differentiator followed by a bandpass filter with −3-dB points at 0.2 and 350 Hz (Fig. A3). The analog signal is further filtered (four-pole Butterworth) at 64 Hz (−3 dB) prior to sampling at 204.8 Hz. The time series is then calibrated, detrended, and windowed over 512 points before a Fourier transform is performed. A response function to correct for the attenuation of the antialiasing filter is applied in the frequency domain (Fig. A4).

Complete resolution of the spectral variance requires resolution of and integration to the Kolmogoroff wavenumber, $k_s = (2\pi)^{-1}(\epsilon/\nu^3)^{1/4}$ cpm. This is not usually possible using airfoil probes since they cannot resolve sufficiently small scales except at the smallest measured oceanic values of ϵ. Partial correction for the incomplete spatial resolution of the probes is made using the wavenumber response transfer function determined by Ninnis (1984) by

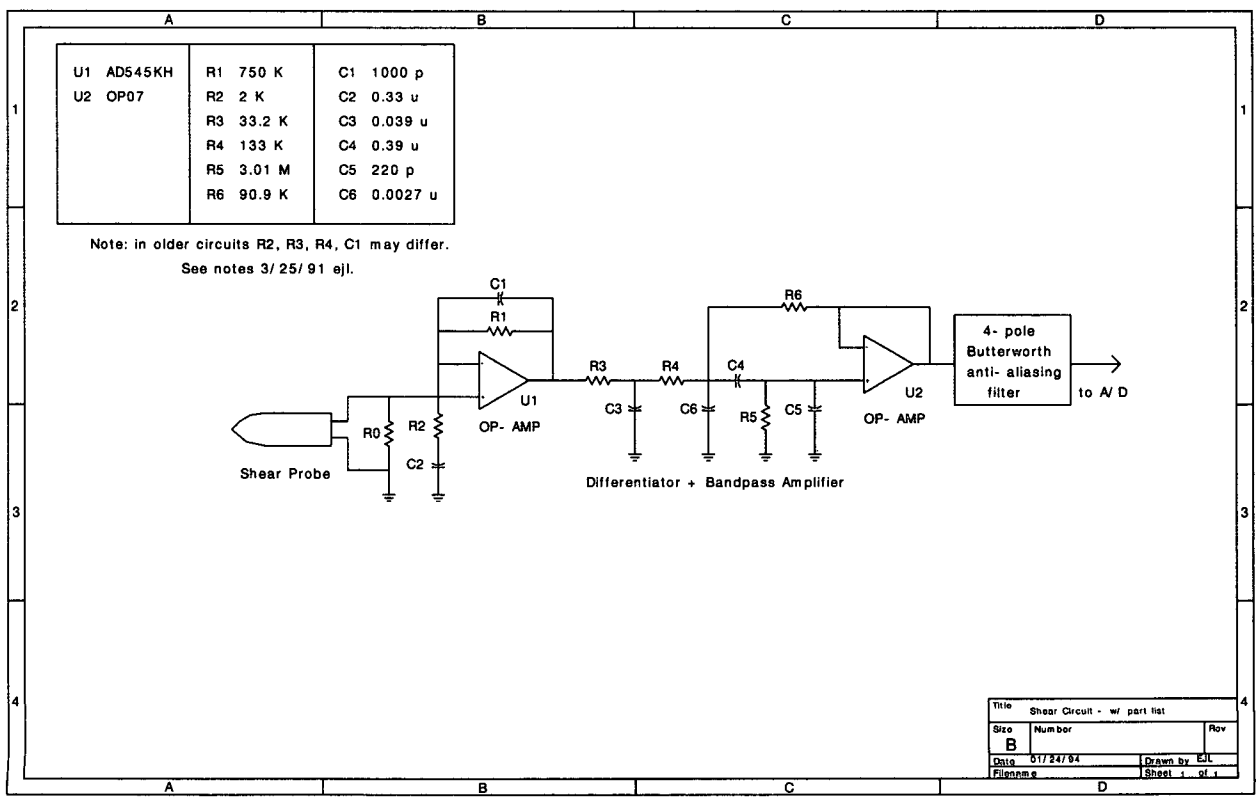

FIG. A3. Schematic of the circuitry used with the OSU airfoil probes.

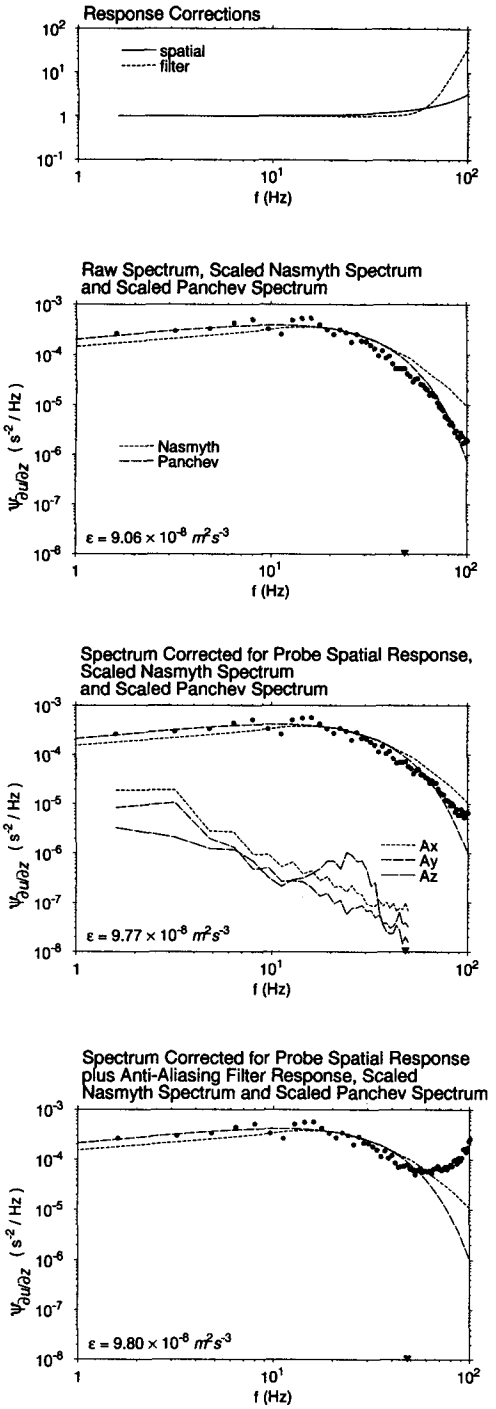

FIG. A4. (a) Typical CHAMELEON spectrum and spectral processing as outlined in appendix A. The upper panel shows the form of the response corrections for the antialiasing filter (dashed) and for the spatial rolloff of the airfoil probe. The second panel shows the raw spectrum as well as both the Nasmyth empirical spectrum and the Panchev–Kesich theoretical spectrum, both scaled according to the estimate of ϵ obtained using the correction for incomplete resolution of the spectrum. The inverted triangle on the abscissa indicates the upper integration limit. The estimate for ϵ is 9.06×10^{-8} m^2 s^{-3}. The third panel shows the spectrum after the spatial response correction has been applied. The new estimate of ϵ is 9.77×10^{-8} m^2 s^{-3}. Also shown are spectra computed from three accelerometers mounted orthogonally inside of the CHAMELEON electronics package; these have been converted to equivalent shear spectra, $\psi^{acc}_{\partial u/\partial z} = \psi_{acc}/W^2$, where W is the fall speed. The bottom panel shows the spectrum after the spatial response and the filter response corrections have both been applied. The final estimate of ϵ is 9.80×10^{-8} m^2 s^{-3}.

comparison of turbulence spectra measured simultaneously by laser Doppler anemometry and Osborn's shear probes in grid turbulence set up in a water tunnel. This is

$$T\left(\frac{k}{k_0}\right) = \sum_{n=0}^{4} a_n \left(\frac{k}{k_0}\right)^n, \qquad \text{(A5)}$$

where k is cyclic wavenumber, k_0 is 170 cpm, $a_0 = 1.000$, $a_1 = -0.164$, $a_2 = -4.537$, $a_3 = 5.503$, and $a_4 = -1.804$. The inverse of (A5) is shown in Fig. A4. However, the spectrum is attenuated at high frequencies to such an extent that noise dominates (conversion to cyclic wavenumber corresponds to $k = f/W$, where W is the mean flow speed past the sensor; usually, W is taken to be the descent rate of the profiler w). Hence, the spectrum cannot be completely corrected for incomplete spatial resolution at the highest frequencies (wavenumbers).

As a model for the turbulence spectrum in sufficiently energetic regions of the ocean, we use the form determined by Nasmyth (1970) (use of an alternate form is discussed in appendix C). This "universal" form indicates that 90% of the variance is resolved by integrating to $0.5k_s$. This is then used as a prescription for both setting integration limits of the spectrum and correcting the variance for incomplete spectral integration. Corrected spectra (with filter and spatial corrections applied) are first integrated over the wavenumber range 2–10 cpm. The first estimate of dissipation rate is made from the spectral variance according to (2), and k_s is computed. The spectral integration limits are then adjusted according to the value of k_s and minimum and maximum acceptable integration limits. The maximum acceptable integration limit ensures that integration is not continued into the noise-dominated region of the spectrum at high frequencies. The minimum acceptable integration limit ensures a finite integration band and effectively sets the noise level of the computation at low signal levels (a noise spectrum is shown in Fig. A5). The following steps determine the integration limits:

1) if $0.5k_s < 10$ cpm, integration is stopped at 10 cpm;

2) if $0.5k_s > 45$ cpm, integration is stopped at 45 cpm;

3) if $10 < 0.5k_s < 45$ cpm, integration is stopped at $0.5k_s$.

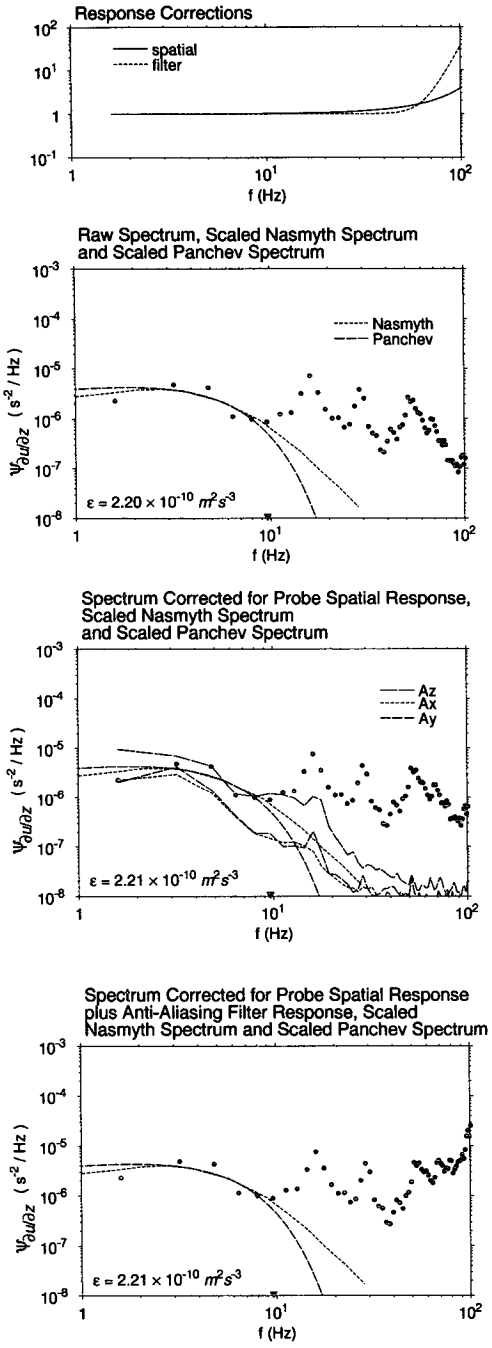

FIG. A5. Noise-level shear spectrum. In this case the upper integration limit is 10 cpm. The contamination of the spectrum by vehicular motion is represented by the accelerometer spectra shown in the third panel. The variance of ψ_{acc}/W^2 integrated to 10 cpm is approximately equivalent to that determined by integrating the shear probe spectrum to 10 cpm.

Because integration of the spectrum does not extend to k_s, the full variance is not resolved. To correct for this, an iterative correction scheme is employed. The universal spectral coefficients are scaled to dimensional units using Kolmogoroff scaling (Tennekes and Lumley 1972), and the first estimate of ϵ obtained as above. The variance of the universal spectrum in the integration band is determined by integrating over the wavenumber limits used to make the first estimate of ϵ. This is then compared to the variance of the corrected data spectrum over the same band. If these two estimates agree to within 5%, the result is accepted. If not, the estimate of ϵ is corrected by multiplying by the ratio of the measured to the universal curve estimates of ϵ. New integration limits are determined according to the rules listed above, and the full procedure is then iterated until agreement to within 5% is achieved over the specified integration band. The final estimate of ϵ is that obtained by integrating the properly scaled universal spectrum to k_s (see appendix C).

Because the winch is free wheeling, occasional operator errors result in inadvertent line glitches, transferring tension to the cable, which is sensed at the shear probes on CHAMELEON as it falls. This is detected by three accelerometers mounted orthogonally on CHAMELEON. Estimates of ϵ are flagged and not included in further computations whenever the rms value of the vertical accelerometer exceeds a fixed threshold level. (The threshold level may vary depending on the experiment—for example, measurements in the tidal channels of British Columbia show extremely high values of ϵ in the midst of turbulent flows with length scales ranging from 0.01 to 100 m. CHAMELEON is buffeted by the flow itself, but because the signal level is proportionately higher, the buffeting-induced contribution is buried in the signal—hence, a higher threshold level is used in this instance.)

Another contaminant to the shear probe measurements is encounters with detritus or plankton in the water column. This usually appears as a short-lived glitch in the record, easily distinguished from fluid turbulence as it generally appears on one probe but not the other since the particle sizes are so much smaller than the probe separation ($\approx$0.015 m). We remove these from final ϵ computations by simply using the smaller estimate (from the two probes) where they differ by more than a factor of 10. Both of these error-flagging procedures are evident in the summary plot of CHAMELEON 3648 (Fig. A6). Because inevitable problems often remain in the data even after these objective screenings, the data are routinely examined subjectively by plotting them in various ways.

d. Uncertainties

Uncertainties associated with estimating ϵ have been discussed thoroughly by Oakey (1982), Lueck et al. (1983), Moum and Lueck (1985), and Peters et al. (1988). These are briefly listed here. Random uncertainties are due to the following:

1) Unknown flow-rate variations past the sensors. Since ϵ depends on the fourth power of the flow rate,

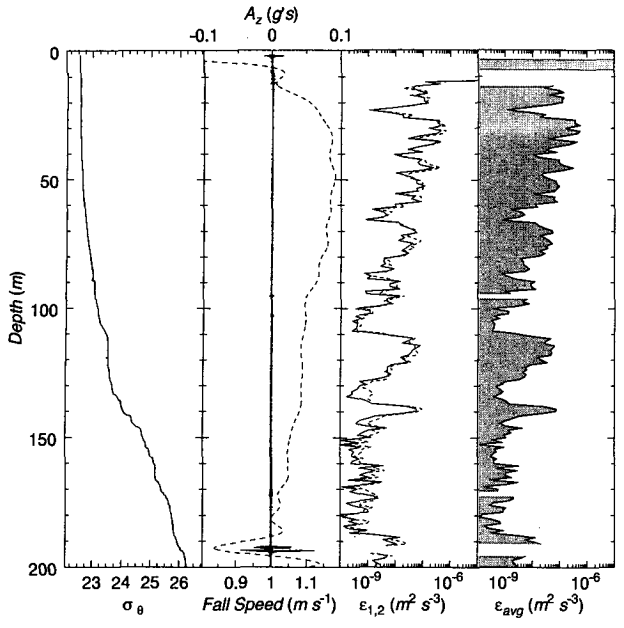

FIG. A6. Summary plot of CHAMELEON profile 3648. This particular example is an especially good example of the types of problems associated with making ϵ measurements and was chosen to show the application of error corrections used in arriving at the estimate of ϵ. At the top of the profile, the data/tether line did not go out smoothly as determined by the vertical acceleration sensor A_z (solid line, panel 2) and the slow adjustment to terminal fall speed. The fall speed (dashed line, panel 2) increased to about 1.15 m s^{-1} at 30 m, then decreased with depth to less than 1 m s^{-1} by 190 m, at which point a strong line glitch was detected in A_z. This may have been due either to winch operator error or shark encounter and is an extreme and rare example. The data are flagged in the estimate ϵ_{avg} and not used for further analysis. Similar, though smaller, glitches were detected at 95 and 182 m; although the apparent effect here is small in $\epsilon_{1,2}$, the data are flagged in ϵ_{avg}, as shown (this becomes especially important when making low-noise measurements deeper in the main thermocline). At 133 m, $\epsilon_2 > 10\epsilon_1$ and ϵ_{avg} is replaced by ϵ_1. Inspection of the raw data signal indicates a spike in the signal $\partial u/\partial z_2$, likely due to a plankton encounter.

this is critical. Generally, we estimate the flow rate as the fall speed of the profiler. Where the vertical velocity of the water is everywhere zero, and the profiler falls vertically with no tilt angle, the fall speed is equivalent to the flow speed. However, these assumptions are generally untrue to some unknown extent. Vertical velocities associated with internal gravity waves, for example, may vary by $O(10^{-2})$ m s^{-1} over several meters vertically; we do not know the local response of the profiler to this velocity change. As well, CHAMELEON routinely tilts 1° with a period of about 7 s; however, since we do not know whether the body follows a vertical path or its nose, we cannot correct for the relative change in flow speed.

In energetic flow regimes like the British Columbian tidal channels, where vertical velocities of 1 m s^{-1} are frequently associated with vertical scales of tens of meters, we have mounted a small electromagnetic velocity sensor on CHAMELEON specifically to ensure that we know the flow speed very well. In most open ocean regimes, and away from the surface, this is not a serious problem.

2) The variance-loss correction scheme used to correct individual spectra for incomplete resolution of the turbulence spectrum. Averages over many spectra are well behaved and are in general agreement with a universal form (Figs. A5 and B6). However, individual spectra deviate substantially from this form. Further, there is more than one universal form to consider (appendix C).

Systematic uncertainties are due to the following:

1) Calibration uncertainty. Uncertainties in calibration can be systematic for all probes done in a single batch (for example, if the flow speed sensor is in error). Random calibration uncertainties can be due to improper alignment of the probes with the flow, which is a factor in each individual probe run. Inaccuracy in the sensitivity calibrated for a single probe will cause a systematic uncertainty in all of the ϵ values estimated from measurements made using that probe.

2) Deviations in electronics transfer functions from design values (which is why they should be measured).

3) Uncertainty in measurement of temperature causing an uncertainty in the estimate of $\nu(T)$.

There are two other factors that contribute to the uncertainty in the estimate of ϵ that we should classify as sampling uncertainties rather than instrumentation uncertainties. As we have already mentioned, there is the problem of determining ϵ in stratified turbulence using the isotropic formulation. The resolution to this problem requires measurement of all twelve components in (1). However, because of the energetic turbulence observed in the upper equatorial ocean, we do not expect this to be a serious limitation here. The other sampling problem involves the real space–time variability of both the turbulence and the background flow field and our limited ability to resolve it with discrete profiles.

We believe the lower limit on estimates of ϵ is due to hydrodynamically induced vibrations by the flow past the body and sensed by the shear probes. The noise level is apparent in probability distributions of ϵ from low signal regions (Fig. 3d). The equivalent noise in ϵ due to body motion is $\int_0^{k_c} \psi_{acc} dk/w^2$ (Moum and Lueck 1985), where ψ_{acc} is the power spectrum of body accelerations. In Figs. A4 and A5, ψ_{acc}/w^2 is plotted together with $\psi_{\partial u/\partial z}$, where $\psi_{\partial u/\partial z}$ is the power spectrum of turbulent shear sensed by airfoil probes. In Fig. A4, the turbulence is sufficiently energetic so that spectral levels of $\psi_{\partial u/\partial z} \gg \psi_{acc}/w^2$ at all frequencies, indicating no contamination of the estimate of ϵ by body motions. Figure A5 represents an example where spectral levels of $\psi_{\partial u/\partial z} \approx \psi_{acc}/w^2$ in the integration band (2–10 cpm). The estimate of ϵ obtained by integration of $\psi_{\partial u/\partial z}$ is 2.21×10^{-10} m^2 s^{-3}, which is approximately that ob-

tained by performing the identical operations on ψ_{acc}/w^2. This indicates the noise level to be due to broadband vehicular vibration. It also suggests how the noise level can be further reduced. If the source of the vibration is hydrodynamic forcing, the energy available must be $\propto w^3$. Indeed, measurements made with CHAMELEON in the main thermocline off northern California with $w = 0.75$ m s^{-1} have noise levels in ϵ smaller by a factor of the cubed ratio of fall speeds, that is, $(1/0.75)^3 \propto 2.4$.

The only other interplatform comparison of ϵ indicated discrepancy between (agreement in) mean values of measurements made from a submarine and those made from a vertical profiler of (within) a factor of 1.8 (Yamazaki et al. 1990), but this was attributed to the natural variability of the turbulence and the differences in horizontal compared to vertical sampling. There is a general agreement among the groups making these measurements that the net sum of all of these uncertainties results in an overall accuracy in mean values of ϵ by something less than a factor of 2. This seems consistent with the only quantitative comparison that has been made to larger-scale dynamics; the ratio of ϵ to the surface buoyancy flux J_b^0 in convectively mixed layers. Shay and Gregg (1986) found ϵ/J_b^0 to be 0.61 for several nighttime cooling cycles in the Bahamas and 0.72 during a cold-air outbreak in a warm-core ring. Anis and Moum (1992) found ϵ/J_b^0 to range from 0.69 to 0.87 for each of six nights of convection at an open ocean site. Imberger (1985) found ϵ/J_b^0 to be 0.45 for convection in the mixed layer of a lake. These are compared to the value of 0.64 estimated for the atmospheric mixed layer (Kaimal et al. 1976; Caughey and Palmer 1979). This range of values suggests that estimates of ϵ made by independent groups are not too far wrong and that an uncertainty in mean values of a factor of 2 is perhaps conservative.

APPENDIX B

The Advanced Microstructure Profiler (AMP)

The intercomparison began 21 November 1991 when R/V *Moana Wave* joined R/V *Wecoma* on station at 0°N, 140°W. From 1419 to 2341 UTC, the University of Washington (UW) group on *Moana Wave* took profiles 9636 to 9667 with AMPs 4 and 5. They then used AMPs 7 and 8 (Fig. B1) to obtain profiles 9674 to 9840. The intercomparison ended at 2304 UTC 24 November when *Wecoma* left the station.

While *Moana Wave* drifted broadside to the wind, AMP was dropped from midships while attached to the ship with a 2.7-mm-diameter flexible tether containing Kevlar fibers having a breaking strength of 2000 N. The tether also contained an optical fiber (Gregg et al. 1982), which transmitted pulses using the Manchester code. The optical pulses were converted to electrical pulses in the rotating drum of the AMP winch and transmitted to the laboratory where the data were displayed and recorded on a Sun-3/150 workstation. When the ship drifted more than 5 km from our station, we recovered the profiler and repositioned upwind.

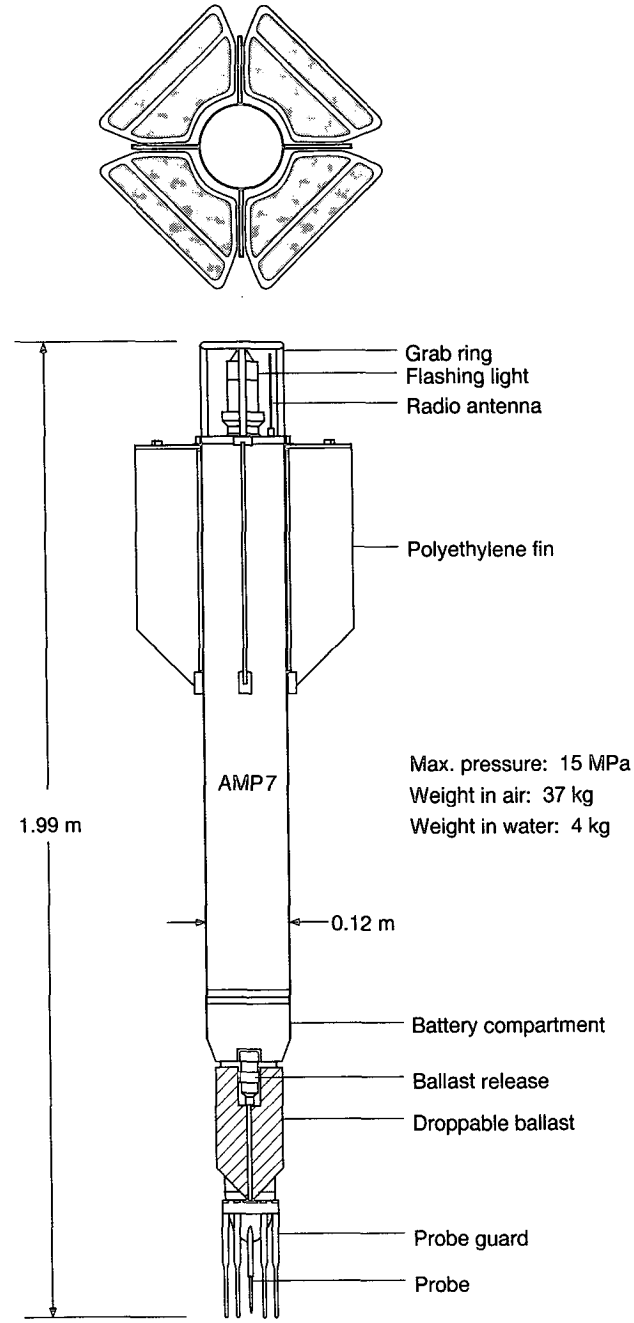

FIG. B1. Schematic of AMP 7 and 8.

In strong shear, drag on the tether exerts significant upward force on loosely tethered vehicles. During Tropic Heat 1, this prevented useful AMP data below about 1.75 MPa. Because the AMP tether cannot be

made thinner, we subsequently minimized the effect of line drag by ballasting AMP more heavily and using drag screens to offset the increased negative buoyancy. For TIWE the AMPs were ballasted 4 kg negative and their fall rate (denoted by w) slowed with hinged drag screens that deploy during descent and fold in during ascent. As a result, drops began at $w = 0.7$ m s^{-1} and ended at 2 MPa with $w = 0.4$ m s^{-1}.

a. Probes and calibration

The airfoil probes used on AMP are constructed in the manner developed by Oakey (1977) and shown in Fig. B2. One end of a bimorph beam is plotted directly in hard epoxy, and the remainder is encased in the soft rubber tip with a parabolic cross section to provide constant lift for cross velocities u' (Osborn and Crawford 1980). Each AMP carries two airfoils, both oriented with their sensitive axis in the same direction so their outputs can be compared during data editing; impacts of plankton on the probes are major causes of noise, and few impacts are simultaneous on both probes.

The airfoils are calibrated using Oakey's procedure (1977) of placing them in a steady water jet having speed V. Slowly oscillating the probes creates a cross-velocity by changing the angle of attack θ. The output voltage is

$$E_0(t) = S_v\left(\frac{V^2}{2g}\right)\frac{u'(t)}{V}\ (\mathrm{V}), \qquad (B1)$$

where S_v (V m^{-1}) is the probe sensitivity. Owing to the small angles, $u'(t)/V \approx \sin\theta(t)$. In practice, $\theta(t)$ and $E_0(t)$ are sinusoidal, and S_v is determined from their peak amplitudes. As shown below, the probe capacitance C_S also affects gain and must be measured. Probe sensitivities and capacitances measured before and after the cruise typically differed less than 15% (Table 1). Probe 159 was damaged during operations and changed the most, with a 33% decrease in S_v.

We use the dynamic response function measured for airfoils by Oakey (1977),

$$H^2_{\mathrm{probe}}(f, w) = \frac{1}{1 + (\lambda_c f/w)^2}, \qquad (B2)$$

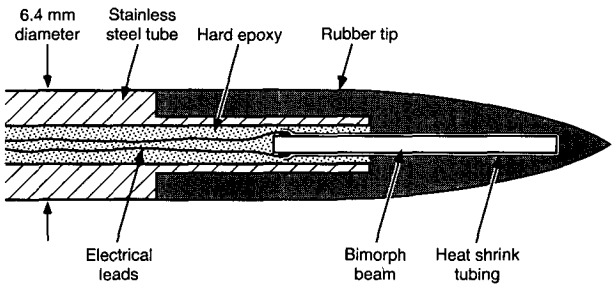

FIG. B2. Schematic of airfoil probe used by the University of Washington group.

TABLE B1. Airfoil sensitivity S_v and capacitance C_S before/after the cruise (UW).

Probe	S_v (V m^{-1})	C_S (pF)
125	26.4/26.2	948.3/935.0
128	23.7/29.4	865.0/842.7
129	26.5/26.2	857.6/838.0
136	30.5/32.0	923.0/897.8
138	23.4/28.4	877.2/847.5
155	25.1/27.0	956.5/915.6
156	26.1/24.9	958.0/940.6
159	26.9/18.1	704.0/640.6
199	26.1/28.8	901.8/886.0
200	25.5/27.5	926.0/912.9
204	29.1/30.0	993.0/983.8
210	30.8/30.6	972.0/966.5
221	26.3/29.1	1024.4/1009.8
223	26.0/30.5	926.2/890.5
242	25.0/22.9	971.4/955.4
249	25.3/29.5	969.9/952.4

with $\lambda_c = 0.02$ m and $f/w = k_3$, which is the vertical wavenumber in cycles per meter.

b. Signal conditioning

The airfoil output voltage E_0 is fed into three sequential circuits that amplify and high-pass the signal (Fig. B3). The first is a charge-sensitive amplifier whose output matches its input voltage while supplying the current needed to drive the second stage. The power transfer function of the charge amplifier is

$$H^2_{\mathrm{ca}}(f) = \frac{(C_S/C_F)^2(f/f_L)^2}{[1 + (f/f_L)^2][1 + (f/f_H)^2]}, \qquad (B3)$$

where $C_F \approx 10^{-9}$ F, $f_L \approx 0.05$ Hz, and $f_H \approx 32$ kHz. The response is unity at frequencies resolved by the airfoil probes and rolls off at lower and higher frequencies.

The second stage establishes the gain and differentiates frequencies less than 100 Hz,

$$H^2_{\mathrm{diff}}(f) = \frac{K^2 f^2}{(F_1^2 + f^2)(F_2^2 + f^2)}, \qquad (B4)$$

where $K = (2\pi R_{\mathrm{D1}} C_{\mathrm{DF}})^{-1} = 77\,629$ Hz, $F_1 = 198$ Hz, and $F_2 = (2\pi R_{\mathrm{DF}} C_{\mathrm{DF}})^{-1} = 387$ Hz.

The third stage sets the gain with

$$H^2_{\mathrm{gain}}(f) = \left(\frac{R_{\mathrm{GF}}}{R_{\mathrm{GI}}}\right)^2, \qquad (B5)$$

where $R_{\mathrm{GF}} = 40.2$ kΩ and $R_{\mathrm{GI}} = 10$ kΩ, to give $H^2_{\mathrm{gain}}(f) = 16.16$.

Finally, a six-pole Tchebyscheff filter has unity gain, with less than 0.2-dB ripple, in the passband and rolls off very sharply at 150 Hz to prevent aliasing. Its power response is

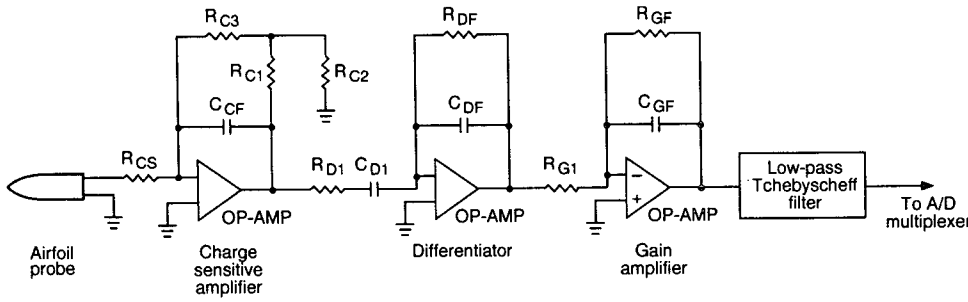

FIG. B3. Schematic of the circuitry used with the UW airfoil probes.

$$H^2_{\text{Tc}}(f) = \frac{1}{1 + \alpha^2[32(f/f_0)^6 - 48(f/f_0)^4 + 18(f/f_0)^2 - 1]^2}, \quad \text{(B6)}$$

where $f_0 = 150/1.0685 = 140.38$ Hz, and $\alpha = [10^{(0.2/10)} - 1]^{1/2} = 0.217$. The factor of 0.2 is the ripple amplitude (dB).

The net electronic transfer function is the product of the separate components

$$H^2_{\text{electronics}}(f) = H^2_{\text{ca}}(f)H^2_{\text{diff}}(f)H^2_{\text{gain}}H^2_{\text{Tc}}(f). \quad \text{(B7)}$$

It is plotted in Fig. B4 with H^2_{probe}.

Following the Tchebyscheff filter, signals are fed to a multiplexer and a 16-bit analog-to-digital converter that takes ±5 V full scale. Consequently, recorded counts are converted to volts by multiplying by $10/2^{16}$. The data are digitized and recorded at 394 Hz.

c. Calculation of ϵ

To obtain ϵ estimates with regular grid spacings, the data are taken in blocks of 5 kPa (0.5 m). The array is completed with zeros to obtain a length that is a power of 2, typically 512 points. To reduce leakage, a Hanning filter is applied before transforming. After transforming, the raw spectrum is adjusted for the zero padding and multiplied by 8/3 to correct for the Hanning filter. Because shear amplitudes vary greatly within each data block, and the Hanning window strongly suppresses signals near the ends of the block. Successive blocks are offset by 2.5 kPa.

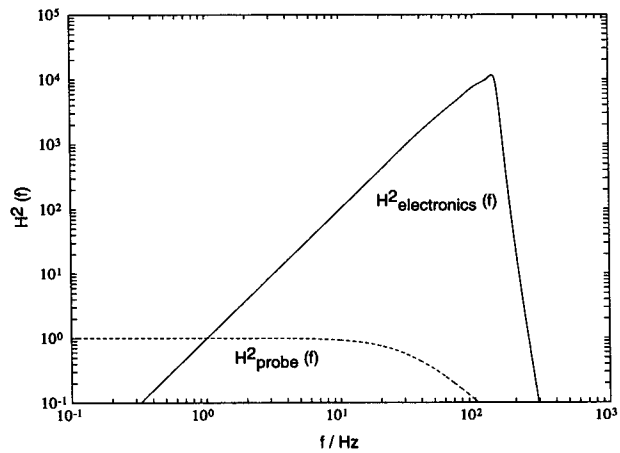

FIG. B4. Power transfer functions of the airfoil probe and of the electronics. Here H^2_{probe} is evaluated for $w = 0.7$ m s^{-1} and is 0.19 at 70 Hz, which corresponds to $k_3 = 100$ cpm.

The spectrum of the recorded data $\Phi_R(f)$ has units of counts squared per hertz. Replacing V with W in (B1), squaring $E_0(t)$ for power, and applying the transfer functions gives the velocity spectrum as

$$\Phi_{\text{vel}}(f) = \frac{(2g/S_v W)^2(10/2^{16})^2}{H^2_{\text{electronics}}(f)H^2_{\text{probe}}(f, w)}\Phi_R(f) \quad (\text{m}^2\,\text{s}^{-2}\,\text{Hz}^{-1}). \quad \text{(B8)}$$

The shear spectrum as a function of vertical wavenumber follows as

$$\Phi_{\text{shear}}(k_3) = (2\pi k_3)^2 w \Phi_{\text{vel}}(f) \quad [\text{s}^{-2}\,(\text{cpm})^{-1}], \quad \text{(B9)}$$

where $k_3 = f/w$. Assuming isotropy of the turbulent velocity fluctuations and integrating then yields the dissipation rate

$$\epsilon = 7.5\nu \int_2^{k_c} \Phi_{\text{shear}}(k_3)dk_3 \quad (\text{W kg}^{-1}). \quad \text{(B10)}$$

Choosing the upper cutoff k_c is the principal difficulty in computing ϵ. Individual spectra have too much statistical uncertainty, and the noise is not sufficiently repeatable to end the integration when $\Phi_r(f)$ drops below a specified level. Instead, the integration is done iteratively by comparing with integrals of Nasmyth's empirical universal spectrum (Oakey 1982). The first integral is cut off at 10 cpm and referred to as ϵ_{10}. A polynomial representation of Nasmyth's spectrum having the same ϵ_{10} is then used to compute k_c as the wavenumber where the universal spectrum is 90% resolved. The observed spectrum is then integrated to k_c, provided it is less than 100 cpm, the nominal probe resolution. When $\epsilon = 10^{-4}$ W kg^{-1}, integrating to 100 cpm returns only 51% of the shear variance. Consequently, higher dissipation rates cannot be accurately measured with airfoil probes. This was not an issue

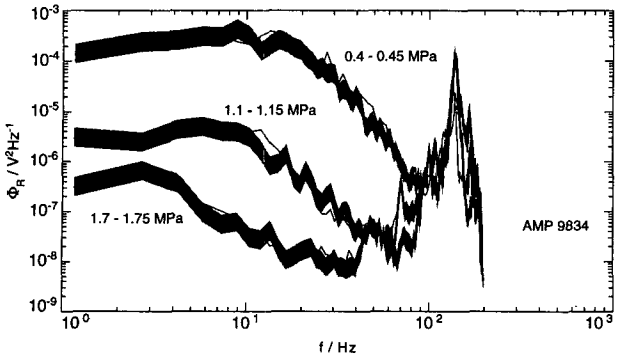

FIG. B5. Spectra of recorded data from three representative pressure ranges in drop AMP 9834 taken at 1342 UTC 24 November 1991. For each pressure range, spectra are plotted for both airfoil probes. The 95% confidence limits (shaded) are for probe 129 (thick line). The thin line represents probe 155.

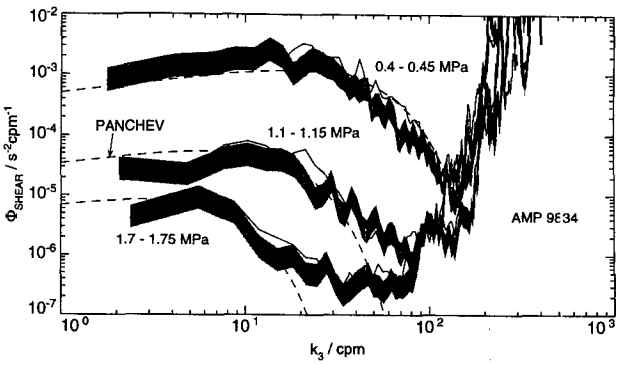

FIG. B6. Shear spectra computed from the recorded spectra shown in the previous figure. From top to bottom the theoretical spectra by Panchev and Kesich (1969) spectra are computed for dissipation rates of 4.37×10^{-7}, 7.40×10^{-9}, and 6.65×10^{-10} W kg^{-1}.

during TIWE, but in more energetic locations we use Nasmyth's spectrum to extrapolate $\Phi_{shear}(k_3)$ beyond 100 cpm (Wesson and Gregg 1994).

Finally, to remove data contaminated with plankton impacts, we compare the two simultaneous ϵ records. Ratios larger than 4 are flagged and the smaller value is used; otherwise the two estimates are averaged.

d. *Typical spectra*

Typically, the recorded spectra $\Phi_R(f)$ decrease strongly in amplitude and high-frequency content with increasing pressure (Fig. B5). Spectra from the two probes generally agree within a factor of 2 at all frequencies. The large peak centered at 138 Hz is produced by excitation of the first bending mode of the pressure tube. By pulling the tether tight and strumming it, the strong shear of the undercurrent excites the resonance, as well as other vibrations. This resonance occurs at 59 Hz in the earlier AMPs used during Tropic Heat 1 (Miller et al. 1989). Increasing the diameters of AMP 7 and 8 to 0.166 m and shortening their lengths to 1.0 m increased the resonant frequency beyond the useful resolution of the airfoil probes.

Shear spectra computed using (B8) and (B9) have similar shapes to $\Phi_R(f)$ to about 30 cpm, where $H^2_{probe}(f)$ begins to affect the corrected spectra (Fig. B6). At higher frequencies, dividing $\Phi_R(f)$ by the electronic transfer function causes the noise to rise even more steeply. The falling shear spectra intersect the noise at 130 cpm for the upper curve and at 80 cpm for the middle one. The bottom curve drops to the noise near 15 cpm, where it is relatively flat and not affected by the antialias filter. The spectral shapes agree approximately with the theoretical forms of Panchev and Keisch (1969) evaluated for the respective $\bar{\epsilon}$, s (Fig. B6).

Figure B7 shows the fall rate w and the final ϵ profile for AMP 9834. To the right are ratios of ϵ from each data channel divided by the final value. The individual channels contain 10–20 spikes that are not coincident and were removed from the final value. Without their removal, vertical averages would be significant overestimates.

APPENDIX C

Comparison of Nasmyth's Universal Turbulence Spectrum and the Panchev–Kesich Form

Integration–correction algorithms for both groups use Nasmyth's empirical spectral form as the model

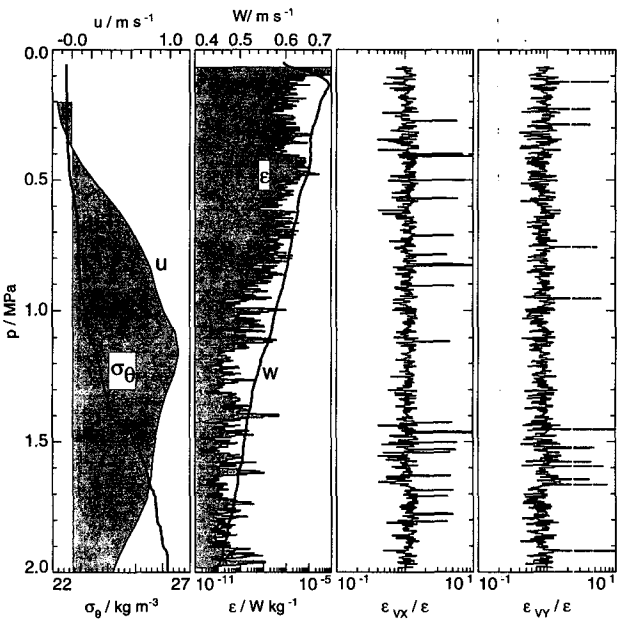

FIG. B7. Summary of AMP 9834. The two panels on the right display ratios of ϵ computed from the two individual channels to the composite value used for the profile. Most spikes rising to large amplitude are not simultaneous at the two channels and are removed during processing.

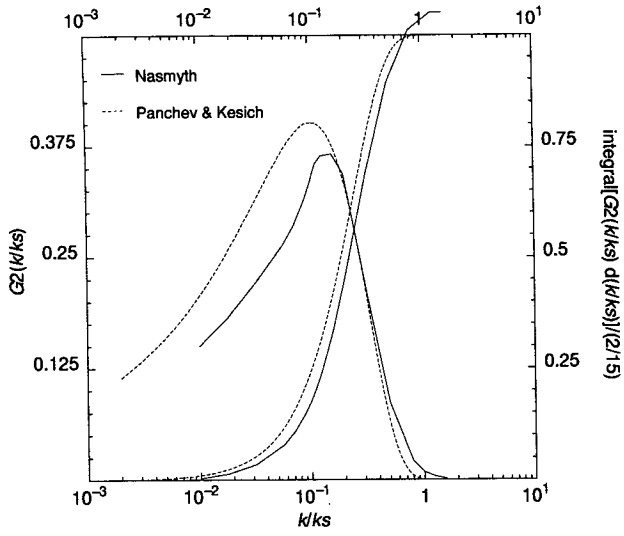

FIG. C1. Comparison of the Nasmyth empirical spectrum and the Panchev–Kesich theoretical form.

for turbulence in the dissipation range of wavenumbers. This is based on data obtained from a towed body in an energetic tidal flow. The nondimensional points (Kolmogoroff scaling) were listed by Oakey (1982) and have been used as a yardstick for comparison of measured spectra obtained in various flow regimes. However, there is no theoretical justification for this particular spectral form and others may work as well. The measured spectra shown in Figs. A4 and B6 have also been compared to the theoretical form derived by Panchev and Kesich (1969), and the agreement is as good or better than that obtained by comparison to the Nasmyth forms. [Seim and Gregg (1994) give the appropriate spectral form for the Panchev–Kesich spectrum.]

It is not our intent here to suggest a preference for one form over any other, nor have we done a systematic analysis to compare measured spectra with the universal forms. This is a topic for further research requiring a careful consideration of the physics involved. For the purpose of making integration corrections based on a universal form, however, it is necessary for us to suppose that either form may be correct and to determine the uncertainty associated with using the same one.

The nondimensional forms of the two universal shear spectra $G_2(k/k_s)$ (Oakey's notation) are plotted against a nondimensional wavenumber in Fig. C1. Also shown are the cumulative values; those obtained by integrating to k/k_s. They are scaled so that they are equivalent to 1 when integrated from $0 \rightarrow \infty$. The Nasmyth form is derived exactly from the points given by Oakey (1982) and integrates to a value slightly greater than 1. Some groups have smoothed the data points and made the integral equal 1. However, this is arbitrary and we choose not to do so here.

The integration–correction algorithms require the measured spectra to match the scaled Nasmyth spectral coefficients over a finite wavenumber range. The variance lost because integration is incomplete is then recovered by integrating the Nasmyth spectral form to ∞. From Fig. C1, we can see that the Panchev–Kesich spectrum has accounted for 96% of the total spectral variance by $0.5k_s$, while the Nasmyth form has accumulated only 90% by $0.5k_s$ (because the Panchev–Kesich form has higher amplitude at low wavenumber and rolls off faster at high wavenumber). Hence, when integrating to $0.5k_s$, the integration–correction algorithms currently used apply a correction factor of $1/0.90 = 1.11$ to the value of ϵ determined by integration of the measured spectrum to $0.5k_s$. If we suppose that the true form ought to be the Panchev–Kesich form, we would have applied a correction factor $1/0.96 = 1.04$. In this case we have overcorrected by 7% of the true value of ϵ.

In flow regimes that are considerably more turbulent than the equator (such as the British Columbia tidal channels or the Strait of Gibraltar), the dissipation spectrum is not well resolved by shear probes, the integration correction is larger, and there is a larger discrepancy between the choice of the two spectral models used to make the correction. However, for the TIWE datasets, it seems that the uncertainty associated with choosing either of these two models is considerably smaller than other factors involved in the estimation of ϵ.

REFERENCES

Anis, A., and J. N. Moum, 1992: The superadiabatic surface layer of the ocean during convection. *J. Phys. Oceanogr.*, **22**, 1221–1227.

Bendat, J. S., and A. G. Piersol, 1986: *Random Data: Analysis and Measurement Procedures.* Wiley, 566 pp.

Caughey, S. J., and S. G. Palmer, 1979: Some aspects of turbulence structure through the depth of the convective boundary layer. *Quart. J. Roy. Meteor. Soc.*, **2**, 811–827.

Gregg, M. C., W. E. Nodland, E. E. Aagaard, and D. H. Hirt, 1982: Use of a fiber-optic cable with a free-fall microstructure profiler. *Oceans '82: Conference Record, Sept. 20–22, 1982,* Marine Technology Society, 283–290.

——, H. Peters, J. C. Wesson, N. S. Oakey, and T. J. Shay, 1985: Intensive measurements of turbulence and shear in the Equatorial Undercurrent. *Nature,* **318**, 140–144.

Hinze, J. O., 1975: *Turbulence.* McGraw-Hill, 790 pp.

Imberger, J., 1985: The diurnal mixed layer. *Limnol. Oceanogr.*, **30**, 737–770.

Itsweire, E. C., J. R. Koseff, D. A. Briggs, and J. H. Ferziger, 1993: Turbulence in stratified shear flows: Implications for interpreting shear-induced mixing in the ocean. *J. Phys. Oceanogr.*, **23**, 1508–1522.

Kaimal, J. C., J. C. Wyngaard, D. A. Haugen, D. R. Cote, Y. Izumi, S. J. Caughey, and C. J. Readings, 1976: Turbulence structure in the convective boundary layer. *J. Atmos. Sci.*, **33**, 2152–2169.

Lien, R.-C., D. R. Caldwell, M. C. Gregg, and J. N. Moum, 1995: Turbulence variability at the equator in the central Pacific at the beginning of the 1991–93 El Niño. *J. Geophys. Res.*, in press.

Lueck, R. G., W. R. Crawford, and T. R. Osborn, 1983: Turbulent dissipation over the continental slope off Vancouver Island. *J. Phys. Oceanogr.*, **13,** 1809–1818.

Miller, J. B., M. C. Gregg, V. W. Miller, and G. L. Welsh, 1989: Vibration of tethered microstructure profilers. *J. Atmos. Oceanic Technol.*, **6,** 980–984.

Moum, J. N., and D. R. Caldwell, 1985: Local influences on shear flow turbulence in the equatorial ocean. *Science,* **230,** 315–316.

——, and R. G. Lueck, 1985: Causes and implications of noise in ocean dissipation measurements. *Deep-Sea Res.*, **32,** 379–390.

——, D. R. Caldwell, and C. A. Paulson, 1989: Mixing in the equatorial surface layer and thermocline. *J. Geophys. Res.*, **94,** 2005–2021.

——, D. Hebert, C. A. Paulson, and D. R. Caldwell, 1992: Turbulence and internal waves at the equator. Part 1: Statistics from towed thermistors and a microstructure profiler. *J. Phys. Oceanogr.*, **22,** 1330–1345.

Nasmyth, P., 1970: Oceanic turbulence. Ph.D. thesis, Institute of Oceanography, University of British Columbia, 69 pp.

Ninnis, R. M., 1984: The effects of spatial averaging on airfoil probe measurements of oceanic velocity microstructure. Ph.D. thesis, Institute of Oceanography, University of British Columbia, 109 pp.

Oakey, N. S., 1977: An instrument to measure oceanic turbulence and microstructure. Bedford Institute of Oceanography, Report Series/BI-R-77-3/May 1977, Dartmouth, Nova Scotia, Canada, 52 pp.

——, 1982: Determination of the rate of dissipation turbulent energy from simultaneous temperature and velocity shear microstructure measurements. *J. Phys. Oceanogr.*, **12,** 256–271.

Osborn, T. R., and W. R. Crawford, 1980: An airfoil probe for measuring turbulent velocity fluctuations in water. *Air–Sea Interactions: Instruments and Methods,* F. Dobson, L. Hasse, R. Davis, Eds., Plenum, 369–386.

Panchev, S., and D. Keisch, 1969: Energy spectrum of isotropic turbulence at large wavenumbers. *Comptes rendus de l'Académie bulgare des Sciences,* **22,** 627–630.

Peters, H., M. C. Gregg, and J. M. Toole, 1988: On the parameterization of equatorial turbulence. *J. Geophys. Res.*, **93,** 1199–1218.

Shay, T. J., and M. C. Gregg, 1986: Convectively driven turbulence in the upper ocean. *J. Phys. Oceanogr.*, **16,** 1777–1798.

Seim, H. E., and M. C. Gregg, 1994: Detailed observations of a naturally occurring shear instability. *J. Geophys. Res.*, **99,** 10 049–10 073.

Tennekes, H., and J. L. Lumley, 1972: *A First Course in Turbulence.* MIT Press, 300 pp.

Thoroddsen, S. T., and C. W. Van Atta, 1992: The influence of stable stratification on small scale anisotropy and dissipation in turbulence. *J. Geophys. Res.*, **97,** 3647–3658.

Wesson, J. C., and M. C. Gregg, 1994: Mixing at Camarinal Sill in the Strait of Gibraltar. *J. Geophys. Res.*, **99,** 9847–9878.

Yamazaki, H., and T. R. Osborn, 1990: Dissipation estimates for stratified turbulence. *J. Geophys. Res.*, **95,** 9739–9744.

——, R. G. Lueck, and T. R. Osborn, 1990: A comparison of turbulence data from a submarine and a vertical profiler. *J. Phys. Oceanogr.*, **20,** 1778–1786.